# nature geoscience



**Article** 

https://doi.org/10.1038/s41561-025-01861-7

# Seismic gap breached by the $2025 M_w 7.7$ Mandalay (Myanmar) earthquake

Received: 25 June 2025

Accepted: 22 October 2025

Published online: 14 November 2025

Check for updates

Bo Li ®¹⊠, Sigurjón Jónsson ®¹, Cahli Suhendi¹, Jihong Liu ®¹, Duo Li ®², Arthur Delorme³, Yann Klinger ®³ & Paul Martin Mai ®¹⊠

Seismic gaps are fault sections that have not hosted a large earthquake for a long time compared to neighbouring segments, making them likely sites for future large events. The  $2025 M_w 7.7$  Mandalay (Myanmar) earthquake, on the central section of the Sagaing Fault, ruptured through a known seismic gap and ~160 km beyond it, resulting in an exceptionally long rupture of ~460 km. Here we investigate the rupture process of this event and the factors that enabled it to breach the seismic gap by integrating satellite synthetic aperture radar observations, seismic waveform back-projection, Bayesian finite-fault inversion and dynamic rupture simulations. We identify a two-stage earthquake rupture comprising initial bilateral subshear propagation for ~20 s followed by unilateral supershear rupture for ~70 s. Simulation-based sensitivity tests suggest that the seismic gap boundary was not a strong mechanical barrier in terms of frictional strength, and that nucleation of the earthquake far from the gap boundary, rather than its supershear speed, allowed the rupture to outgrow the gap and propagate far beyond it. Hence, we conclude that the dimension of seismic gaps may not reflect the magnitude of future earthquakes. Instead, ruptures may cascade through multiple fault sections to generate larger and potentially more damaging events.

On 28 March 2025, a magnitude  $M_{\rm w}$  7.7 ( $M_{\rm w}$ , moment magnitude) earthquake occurred near Mandalay, Myanmar's second-largest city, which is inhabited by ~1.2 million people. This extreme temblor ruptured ~460 km along the central Sagaing fault and created widespread destruction throughout Myanmar. Strong ground shaking was also reported in neighbouring countries, notably even in Bangkok at over 1,000-km epicentral distance. The earthquake caused more than 5,000 fatalities and 11,000 injured, and hundreds of people were reported missing.

The Sagaing Fault Zone (SFZ), a right-lateral strike–slip plate boundary between the Sunda and Burma plates, extends over 1,200 km in the north–south direction  $^{1,2}$ . Accommodating about half of the relative plate motion with a variable slip rate of 11-24 mm per year  $^{3-5}$ , it is among the most seismically active faults in mainland Southeast Asia  $^{6,7}$  (Fig. 1a).

In southern Myanmar, the 1930 surface magnitude (M) 7.2 and M7.3 earthquakes ruptured the Bago and Pyu fault sections, respectively<sup>6,8</sup>. The Nay Pyi Taw section hosted an M7 earthquake in 1929 and an  $M_{\rm w}$  6.8 event in 2003<sup>6,7</sup>. To the north, the 1946 M7.7 and 1956 M7.1 earthquakes broke the Sagaing fault section<sup>7,8</sup>, which also hosted the 2012  $M_{\rm w}$  6.8 Thabeikkyin earthquake. In contrast, until the 2025 temblor the Meiktila section had been seismically quiet since 1839, defining an ~220-km-long seismic gap<sup>6,7,9</sup>.

Earthquake cycle theory suggests that faults or fault sections devoid of large earthquakes for many decades or even centuries are probable locations of future events 10. Termed 'seismic gaps', these fault areas are generally identified from historical records, earthquake catalogues, geodetic measurements and field geological investigations 6.11. The seismic gap hypothesis further posits that seismic hazard is lowest immediately after a major rupture, assuming that stress was fully

¹King Abdullah University of Science and Technology (KAUST), Thuwal, Saudi Arabia. ²Earth Sciences New Zealand, Lower Hutt, New Zealand. ³Université Paris Cité, Institut de Physique du globe de Paris (IPGP), CNRS, Paris, France. ⊠e-mail: bo.li.3@kaust.edu.sa; martin.mai@kaust.edu.sa

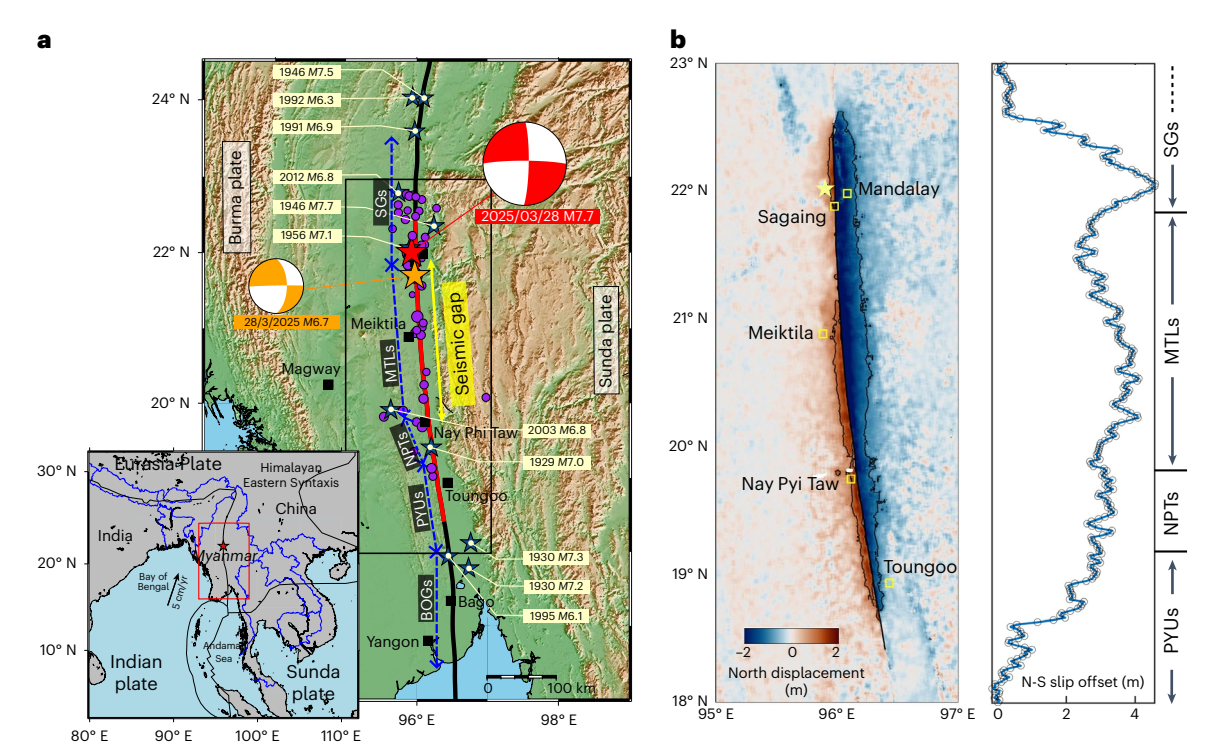


**Fig. 1**| **Tectonic setting and coseismic displacements of the 2025**  $M_{\rm w}$ **7.7 Mandalay earthquake. a**, Tectonic map showing the Sagaing Fault (black line) and its different fault sections<sup>7</sup>, the coseismic surface rupture trace (red line), aftershocks recorded during the month after the event (from the IRIS database; purple circles, scaled by magnitude; range  $M_{\rm w}$  3.5–6.7) and major historical earthquakes (blue stars)<sup>7</sup>. Focal mechanisms of the  $M_{\rm w}$  7.7 mainshock and  $M_{\rm w}$  6.7 aftershock are shown as red and orange beachballs, respectively. The spatial extent of the seismic gap is revised according to ref. 6, taking into account the

 $1929\,M7$  and  $2003\,M_{\rm w}$  6.8 earthquakes in the Nay Pyi Taw section. The black box outlines the area shown in **b**, and the inset map shows the plate-tectonics setting of Myanmar (the red box marks the study area). SGs, Sagaing fault section; MTLs, Meiktila section; NPTs, Nay Pyi Taw section; PYUs, Pyu section; BGOs, Bago section. **b**, Left: north component of the surface displacement derived from Sentinel-1 SAR data. The smooth black line indicates the SAR-mapped fault rupture trace, black contours mark displacement of 1 m, and the yellow star denotes the mainshock epicentre (from IRIS). Right: along-fault surface slip offset.

released coseismically and then increases again interseismically due to long-term tectonic loading  $^{12,13}$ . Based on a seismic gap's areal extent and information on earthquake recurrence time, the seismic gap hypothesis has been used to estimate the dimensions, timing and magnitude of future earthquakes  $^{14,15}$ , although such estimates carry considerable epistemic uncertainty  $^{12,16,17}$ .

The  $2025 M_{\text{w}}$  7.7 Mandalay earthquake challenges the seismic gap hypothesis. The rupture nucleated near the northern edge of the Meiktila seismic gap, propagated through the gap, and then continued even farther for over 160 km beyond its southern boundary, producing an unusually long rupture of ~460 km. Other examples of 'rupture overshoot' include the 2010  $M_{\rm w}$  8.8 Maule earthquake that initiated within the seismic gap and propagated bilaterally beyond it<sup>18</sup>. Similarly, the 2004  $M_w$  9.2 Sumatra-Andaman earthquake ruptured fault areas associated with the 1881 (M7.5), 1881 (M7.9) and 1941 (M7.7) events, forming a continuous rupture zone of ~1,300-km length along the Sunda megathrust<sup>19</sup>. These cases have led to debates on the reliability of identified seismic gaps and their viability in estimating rupture extent and the magnitude of future earthquakes<sup>20</sup>. Understanding the enabling factors for ruptures to break through seismic gap boundaries helps to improve seismic hazard assessment and to better prepare for future large earthquakes in such regions.

# Coseismic rupture imaging A 460-km-long surface rupture

Using interferometric synthetic aperture radar (InSAR)<sup>21</sup> and pixel off-set tracking (POT)<sup>22</sup>, we derived the three-dimensional (3D) coseismic surface-displacement field of this earthquake using the strain model with variance component estimation (SM-VCE) method<sup>23</sup>. The measurements reveal a total coseismic surface-rupture length of ~460 km

(Fig. 1b), with horizontal displacements dominating the displacement field (Extended Data Fig. 1). The horizontal displacement field shows a maximum coseismic surface slip of -4.5 m near the epicentre (at -22° N). The slip-offset amplitude decreases sharply to the north, yielding a rupture extent of -60 km towards north. To the south, the surface displacement initially tapers to -2.3 m at an epicentral distance of 60 km, before increasing again to a secondary peak of 4.1 m near 20.5° N, -160 km south of the epicentre. Surface slip terminates near 18.4° N, resulting in a southward rupture extent of -400 km, so the overall rupture length is -460 km.

The north displacements are asymmetric across the fault, particularly along the northern surface rupture (Fig. 1b). To the south, this asymmetry becomes less pronounced and the zone of coseismic surface deformation becomes narrower. These displacement patterns are confirmed by optical satellite image correlation (Extended Data Fig. 2). Together, our results indicate along-strike variations in the fault geometry, suggesting a shallower fault dip but deeper fault slip towards the north.

### Rupture complexity from back-projection

To map the coseismic rupture evolution, we applied back-projection using three global seismic arrays (Supplementary Fig. 1) in different frequency ranges (Fig. 2a). Our results reveal simultaneous bilateral north-to-south rupture propagation in the initial -20 s. To the north, the rupture propagated with an average rupture velocity of  $V_{\rm R} \approx 3~{\rm km~s^{-1}}$  and ceased -60 km from the epicentre. By contrast, southward rupture continued for longer, transitioned from a subshear to supershear  $V_{\rm R}$ , and sustained the supershear rupture for an additional -70 s with an average velocity of -4.8 km s<sup>-1</sup> (Fig. 2b). The total rupture duration was -90 s over a distance of -460 km, consistent with the SAR image observations.

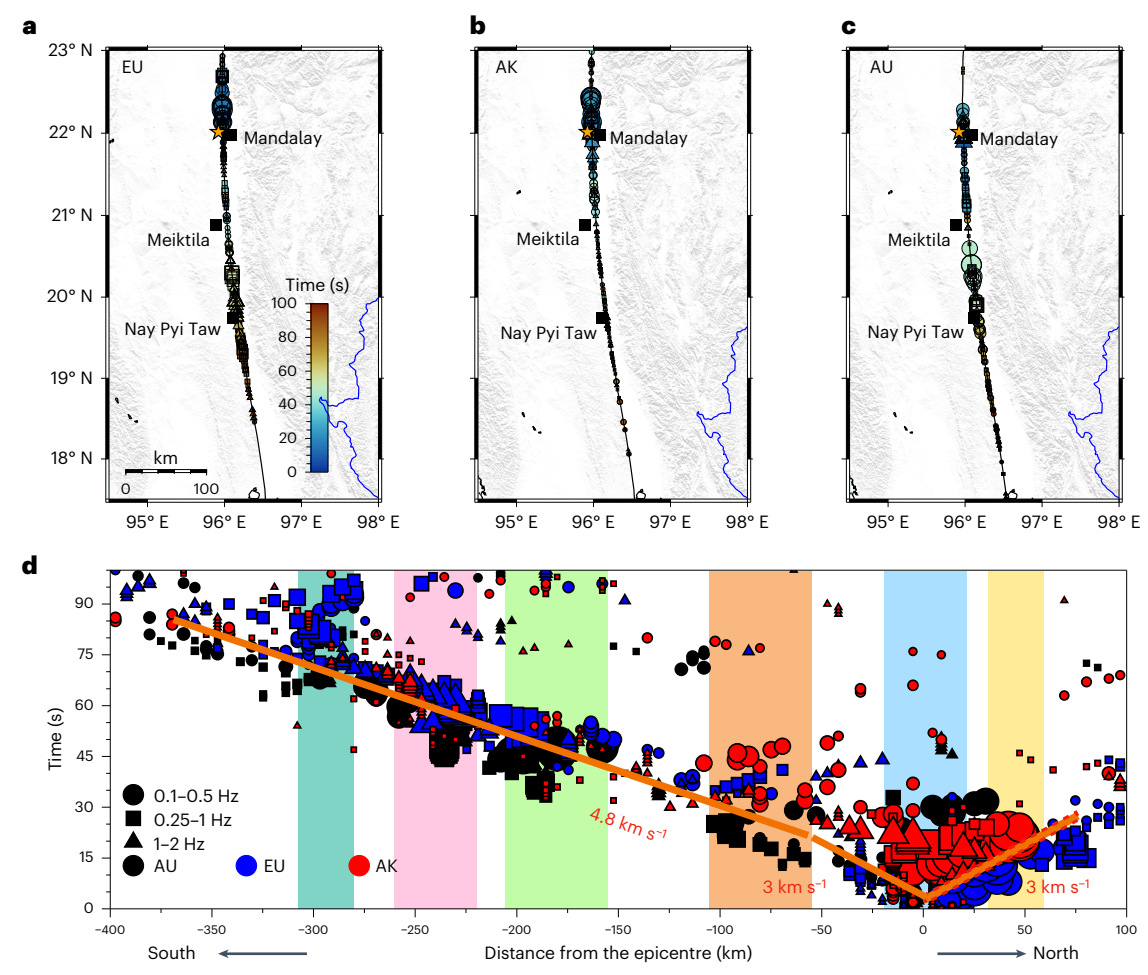


**Fig. 2** | Array- and frequency-dependent back-projection for the 2025  $M_w$  7.7 Mandalay earthquake. a–c, Back-projection using the European Array (EU) (a), Alaskan Array (AK) (b) and Australian Array (AU) (c), respectively. Different symbols represent different frequency bands (shown bottom left, d). Symbol size corresponds to the relative peak beam power within each frequency band, and

colours indicate rupture timing.  $\mathbf{d}$ , Rupture distance as a function of time, with solid orange lines denoting the average rupture propagation. Colour-shaded regions highlight distinct clusters of high-frequency radiation inferred from the back-projection.

The back-projection results reveal frequency- and arraydependent high-frequency seismic-radiation sources (Fig. 2a), indicating effects of the rupture directivity and space-time complexity of the rupture process<sup>24</sup> (Methods). Several distinct high-frequency radiation clusters are observed (Fig. 2b). The first cluster (blue-shaded region) around the epicentre (near Mandalay city) marks the initial phase of the rupture. The second cluster (yellow-shaded region) occurs at the northern rupture termination due to a strong rupture-stopping phase. Yet another cluster is observed south of the epicentre (orange-shaded region), coinciding with the subshear-to-supershear rupture-speed transition. This location also shows a change in the surface-slip offset trend, where the fault offset transitions from decreasing to increasing (Fig. 1b). Finally, the three arrays consistently identify a cluster of strong seismic radiation near Nay Pyi Taw, suggesting a pronounced change in rupture behaviour. This area marks the southern boundary of the seismic gap, suggesting a localized variation in stress conditions and/or change in fault geometry.

# Rupture process modelling

#### Bayesian finite-fault estimation

For kinematic and dynamic rupture modelling, we define the fault geometry using the coseismic surface displacements derived from SAR image observations and optical image correlation (Fig. 1b and

Extended Data Fig. 2). The data define an almost linear surface-rupture trace, with a minor eastward bend 190 km south of the northern-most rupture. Therefore, we represent the surface-rupture trace by two fault segments, labelled FP1 and FP2, which we elongate slightly to fully capture the coseismic fault slip. Segment FP1 has a strike of 358° and a length of 200 km, and segment FP2 strikes 352° and extends for 320 km. As aftershock data are sparse, we combine geodetic (Fig. 1b and Extended Data Fig. 1) and seismic observations (Supplementary Fig. 2a) for Bayesian estimation of the fault dip and width, as well as average slip. Our results indicate that segments FP1 and FP2 dip eastward at -70° and -80°, respectively (Extended Data Fig. 3). This result aligns with the northward-increasing asymmetry observed in the SAR data (Fig. 1b).

Based on inferred fault geometry, we performed Bayesian estimation to determine the coseismic on-fault slip from 3D surface displacements and teleseismic data. Like the back-projection, the joint inversion (Fig. 3a) reveals two distinct rupture stages: rupture begins bilaterally with an initial rupture speed of ~3.3 km s<sup>-1</sup>; northward rupture stops after 20 s while southward rupture accelerates during the second stage to ~4.6 km s<sup>-1</sup> and then terminates at the northern portion of the Pyu fault segment (PYUs) after ~90 s. Large slip patches are found near the epicentre in the north and along the Meiktila section (MTLs)—the unbroken seismic gap for nearly two centuries<sup>7</sup>—with peak slip reaching ~5 m. To the south, slip decreases

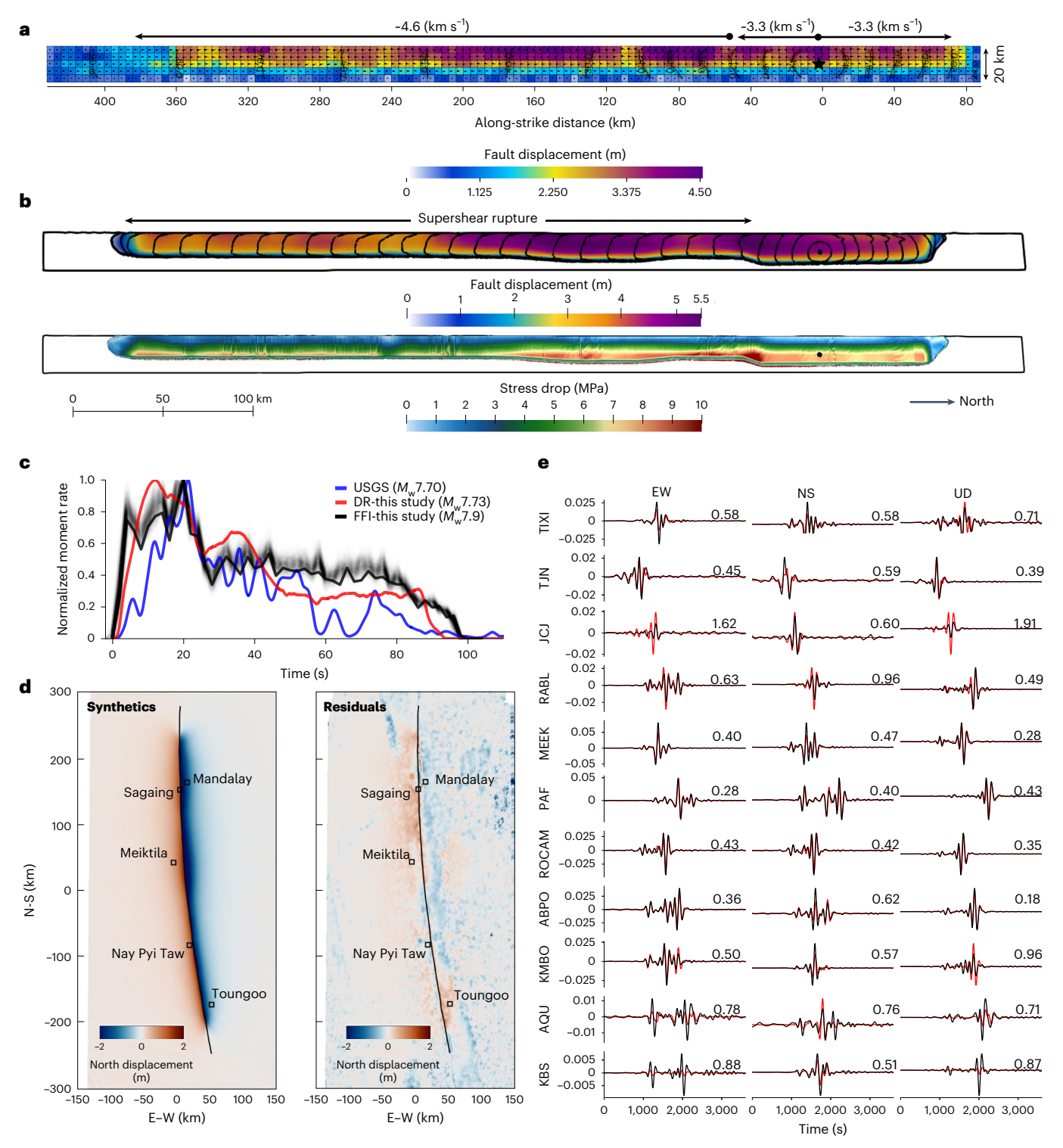


**Fig. 3** | **Kinematic and dynamic models for the 2025**  $M_w$  **7.7 Mandalay earthquake. a**, Final fault slip from the kinematic Bayesian finite-fault inversion. **b**, Final slip of the dynamic rupture simulation (with 3-s rupture-time contours) and associated stress drop. **c**, Normalized MRFs from the Bayesian inversion (including grey-shaded uncertainty bands), dynamic rupture simulations (DR) and the USGS kinematic finite-fault inversion (FFI). **d**, Predicted surface displacements (north) from the dynamic rupture simulation and corresponding residuals relative to the observed data (Fig. 1b). **e**, Teleseismic waveform

comparison (filter range, 100-500 s), with black and red lines showing recorded and synthetic waveforms from the dynamic rupture simulation, respectively, for the east—west (EW), north—south (NS), and up—down (UD) components. For each station, the root mean square (RMS) misfit for each component is shown to the right of the waveforms. The higher misfit at stations KBS and JCJ is probably due to the combined effects of rupture directivity, unfavourable station azimuth (opposite to rupture propagation) or near-nodal planes, and unmodelled 3D velocity heterogeneity  $^{(43,4950)}$ .

and becomes gradually shallower. The Bayesian joint inversion achieves a good fit to local surface displacement and teleseismic waveform data (variance reduction of 78% and 50%, respectively; Extended Data Figs. 4 and 5).

#### Rupture dynamics and ground-motion characteristics

To investigate the physical rupture process, we constructed a fault geometry model based on the SAR image data, Bayesian fault estimation and previous GNSS studies (Methods), and set the prestress

loading conditions (Extended Data Fig. 2c). The fault is embedded in a 3D seismic velocity structure<sup>25</sup> (Supplementary Fig. 3) that comprises pronounced velocity anomalies along the fault and relatively higher velocities to its east.

Our dynamic simulations generate rupture behaviour consistent with the back-projection analysis and Bayesian finite-fault estimation (Fig. 3). Rupture initiates near Mandalay and propagates bilaterally to the north and south. The moment rate function (MRF) reaches its first peak at ~12 s. After ~15 s, southward rupture experiences a subshear-to-supershear transition (visualized by the widening spatial interval between successive rupture time contours; Fig. 3b) that coincides with decreasing surface-slip in the SAR data (Fig. 1b). The northward rupture ceases after ~23 s (note the visible trough in the MRF). Subsequently, southward rupture features a high-slip asperity that produces a second MRF peak near ~35 s, before it traverses the southern edge of the Meiktila seismic gap at ~55 s (marked by a slight decrease in MRF amplitude). Subsequently, the MRF stabilizes and the sustained supershear rupture propagates steadily until it stops at ~90 s. Our dynamic rupture models has an average slip of 3.73 m and mean stress drop of 4.74 MPa.

The on-fault slip distribution of the dynamic rupture model and MRF evolution are consistent with the Bayesian inversion (Fig. 3a-c), albeit the two modelling approaches use entirely different data and methods. Two dominant slip patches are evident, near the hypocentre and -160 km to the south, accompanied by several smaller patches even farther south. The peak slip in the dynamic model reaches -5.8 m, comparable to the 5 m estimated in the Bayesian inversion. The resulting synthetic teleseismic waveforms show good agreement with observations across all azimuths, both in timing and amplitude (Fig. 3e and Supplementary Fig. 2). The dynamic rupture model reproduces the observed SAR surface displacements (Fig. 3d), capturing the larger slip to the north and a secondary slip patch located -160 km to the south.

Synthetic shake-maps of peak ground velocity for the  $2025 M_w 7.7$ Mandalay earthquake depict a highly heterogeneous ground-motion distribution along and across the fault (Extended Data Fig. 6). This variability reflects lateral seismic velocity contrasts, with lower velocities on the western side result in stronger ground motions. Supershear rupture amplifies off-fault shaking, whereas subshear creates strong amplification due to rupture directivity (Extended Data Fig. 6a,c). Despite differing rupture styles, both scenarios exhibit attenuation trends consistent with empirical ground-motion models<sup>26-29</sup> (Extended Data Fig. 6b.d). Remarkably, even though the supershear scenario yields slightly lower shaking intensities within the near-fault zone compared to the subshear scenario (Extended Data Fig. 6b,d), it shows reduced attenuation and hence elevated amplitudes at greater distances. This increased far-field shaking within the supershear Mach cone  $^{30,31}$  and locally low seismic-wave velocities contributes to the widespread damage even hundreds of kilometres away from the fault.

# Dynamic rupture breaches seismic gap

Our comprehensive data analyses and dynamic rupture simulations collectively confirm that the  $2025\,M_{\rm w}$  7.7 Mandalay earthquake ruptured beyond the Meiktila seismic gap on the central Sagaing fault. It overshot the seismic gap for ~160 km before terminating in the south and thus generated an unusually long strike–slip rupture  $^{32}$ . Thus, questions arise regarding the conditions for such extreme rupture dynamic processes. Are they unique? Can they occur on other continental strike–slip faults? Can we infer initial and boundary conditions that may lead to such behaviour? Understanding the factors that arrest rupture or enable it to extend beyond seismic gaps helps to improve seismic hazard assessment for large continental strike–slip faults.

The fault geometry, nucleation location, geological setting, rupture history and interseismic loading that determine the corresponding on-fault heterogeneous prestress strongly affect the rupture dynamics, thereby controlling rupture extent and earthquake magnitude  $^{33-36}$ .

The Mandalay earthquake ruptured northward for ~60 km from the epicentre, ending near the source region of the  $2012\,M_{\rm w}6.8$  Thabeikkyin earthquake. This termination coincides with (1) a geometric transition  $^{37}$  from a straight fault segment to a zone with two parallel branches and (2) a shift in geologic setting, from post-Pliocene alluvial fans to the volcanic Singu basalts  $^{7}$ . To the south, the earthquake rupture ceased between the Pyu and Bago fault sections, near a clear  $10^{\circ}$  change in fault strike  $^{7.38.39}$ . In addition, Coulomb stress-transfer modelling of major historical earthquakes in the region suggests that the rupture endpoints align with areas of Coulomb stress reduction  $^{9}$ .

Supershear rupture on strike–slip faults has been inferred previously<sup>40,41</sup> and is commonly associated with relatively simple fault geometries<sup>42</sup>. With a rupture speed faster than the shear-wave velocity, supershear ruptures produce a distinct radiation pattern, ground-motion features and dynamic effects compared to subshear ruptures<sup>30,31,43</sup>. Among known events, the 2025 Mandalay earthquake stands out as the longest supershear rupture observed, with sustained supershear propagation for ~350 km.

#### Stress barrier sensitivity tests

To assess the potential for triggering and sustaining supershear rupture beyond the Meiktila seismic gap (Fig. 4a), we conducted a series of dynamic rupture simulations under systematically reduced prestress loading and increased the lateral width of the stress barrier at the southern edge of the seismic gap (all other model parameters remain unchanged; Fig. 4b). Four types of stress barrier (SB1-SB4) were examined. In scenario SB1, the barrier is narrow (~9-km width) and maintains a relatively moderate prestress ratio R (ratio of the fault's dynamic stress drop to its breakdown strength drop,  $R \approx 0.28$ -0.34). In this case, rupture propagates through the barrier and sustains supershear speed beyond it. In scenario SB2, a slightly increased barrier width of 11 km still allows rupture propagation through the stress barrier; however, its rupture mode changes from supershear to subshear (Fig. 4c). Despite identical moment magnitudes, the modified rupture dynamics lead to a redistributed slip pattern with reduced slip amplitudes immediately beyond the stress barrier, followed by higher slip in the forward direction and farther to the south (Fig. 4c). For a wider stress barrier (23 km; scenario SB3), a similar supershear-to-subshear transition is observed, but it occurs earlier along the fault. With further widening of the barrier zone (33 km) and prestress reduction ( $R \approx 0.05-0.3$ ) in the stress barrier (scenario SB4). the rupture is finally arrested.

Our tests illustrate the sensitivity of rupture dynamics to stress heterogeneity. We acknowledge tradeoffs between barrier extent, prestress distribution and other factors not explored in detail here. The observed sustained supershear rupture over a distance of -350 km during the  $M_{\rm w}$  7.7 Mandalay earthquake suggests that the edge of the identified seismic gap does not act as a strong mechanical barrier. In our models, the gap boundary is represented as a stress barrier, potentially linked to geometric complexities or stress adjustment from historical earthquakes, but alternative set-ups may result in a similar, mechanically weaker, barrier.

#### **Nucleation location effects**

Although the fault is geometrically simple, small variations in fault orientation, seismogenic depth and heterogeneous prestress still produce variations in rupture dynamics depending on the nucleation location <sup>33,36</sup>. To demonstrate the effect of nucleation locations and their impact on the rupture-breaching barrier, we compared rupture scenarios with three nucleation locations, one corresponding to the observed hypocentre and two hypothetical cases, at distances of 213, 121 and 66 km northward of the stress barrier. Under identical model set-up and SB1 conditions (Fig. 4b), nucleation closer to the barrier (121 and 66 km) leads to subshear ruptures that reach the barrier and even succeed in breaching it, producing distinct slip patterns, slightly

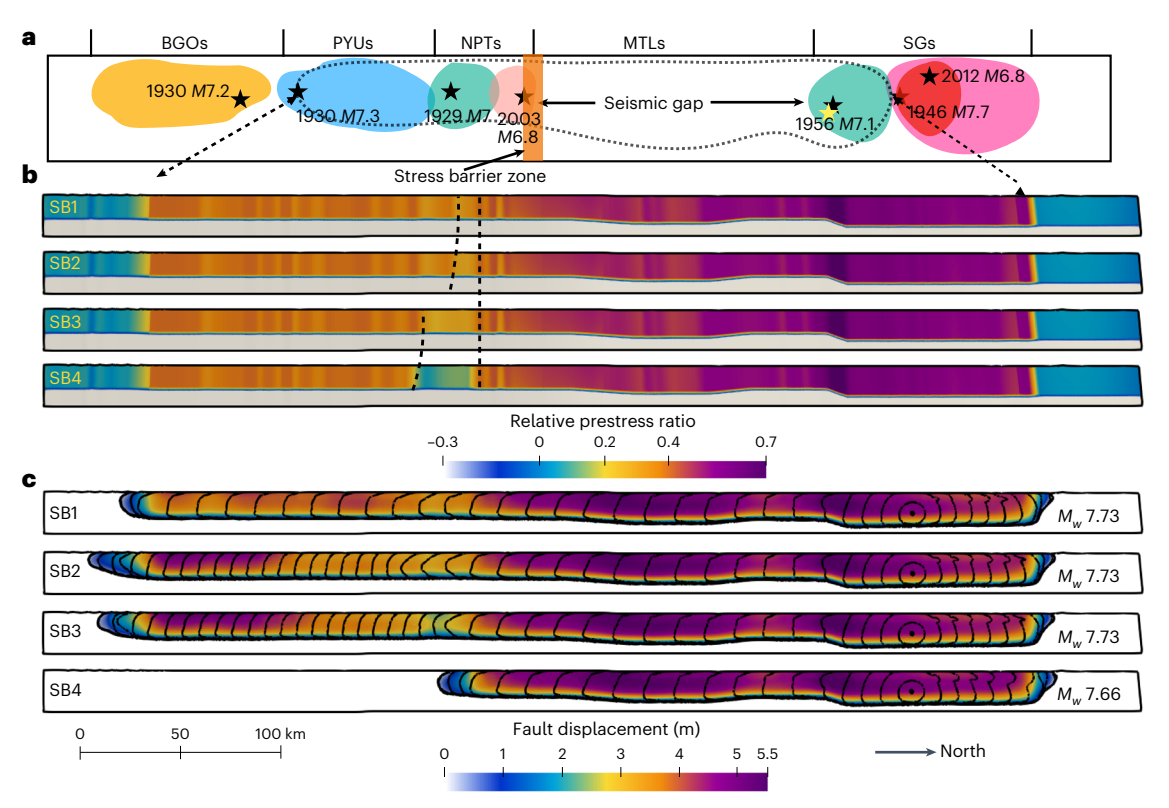


**Fig. 4** | **Testing supershear continuity and triggering potential. a**, Sketch of historical earthquake ruptures  $^7$ , with black stars denoting their hypocentre locations  $^{6.7}$ , and the Meiktila seismic gap on the Sagaing Fault. The yellow star marks the hypocentre of the  $2025\,M_{\rm w}\,7.7$  Mandalay earthquake, and black dashed lines delineate the corresponding rupture zones. The fault is exaggerated in width for visual clarity. Dashed arrows indicate the fault extent shown in **b** and **c**, and the orange-shaded box highlights the stress barrier. **b**, Relative prestress

ratio R of the fault model, modified from the preferred scenario by progressively reducing prestress and expanding the low-stress zone to simulate varying stress barrier strengths (bounded by black dashed lines) at the southern edge of the seismic gap.  $\mathbf{c}$ , Final fault slip for each stress barrier (SB) scenario. Black contours mark rupture fronts at 3-s intervals. The corresponding moment magnitude is shown to the right in each panel.

longer ruptures and marginally larger magnitudes compared to the supershear case that nucleated 213 km away (Extended Data Fig. 7).

To isolate the nucleation-location effect, we adjusted the critical slip-weakening distance  $(D_c)^{44}$  south of and near each nucleation point to ensure ruptures reach the barrier with consistent supershear rupture speed. For model SB1, with prestress loading condition P1  $(R \approx 0.03-0.3)$ , nucleation at 213 km breaches the barrier and maintains supershear propagation; however, nucleation closer to the barrier breaches but transitions to subshear (Fig. 5a-d). Under even further lowered prestress P2  $(R \approx 0.02-0.16)$ , nucleation at 213 km still breaches but becomes subshear beyond the barrier, whereas nucleation at 121 km or 66 km fails to break the barrier (Fig. 5e-h), producing smaller events  $(M_w = 7.65 \text{ and } 7.64)$ . The dynamic histories of the stress ratio (same as R but after rupture initiation) and slip-rate time histories at on-fault receivers (Fig. 5e) show that more distant nucleation produces stronger dynamic stress loading and higher slip rates, enhancing the probability of barrier breaching (Extended Data Fig. 8).

We further examined nucleation effects in model SB4 (Fig. 4b and Extended Data Fig. 9), where supershear rupture nucleated 213 km north is arrested by the barrier. With  $D_{\rm c}$  adjusted for consistent subshear conditions, nucleation at 213 km produces a rupture that crosses the barrier ( $M_{\rm w}$  7.75), with rupture time contours showing clear deceleration within and re-acceleration beyond the barrier. Nucleation at 121 km also breaches the barrier but yields slightly lower slip amplitude and a magnitude of  $M_{\rm w}$  7.72. Nucleation just 66 km away from the barrier fails to cross the barrier and produces the  $M_{\rm w}$  7.66 scenario.

Our sensitivity-testing simulations underscore the critical role of the nucleation location, for both supershear and subshear rupture, in controlling rupture extent, slip distribution and final magnitude. For the given and identical prestress conditions, subshear rupture concentrates more strain energy near the advancing rupture front, whereas supershear rupture radiates a larger fraction of energy towards the Mach-cone zone, producing stronger off-fault ground shaking and deformation 30. Consequently, subshear rupture may be more effective in dynamically driving rupture across a stress barrier under otherwise identical conditions.

At least two factors enabled the  $2025 M_w 7.7$  Mandalay earthquake to rupture beyond the inferred seismic gap. First, the stress barrier at the gap's boundary was insufficiently strong to arrest the rupture. With an estimated recurrence interval of 90-115 years on the Pyu segment and the last major earthquake in this region being in 1930  $(M7.3)^6$ , the 95-year-long interseismic period led to notable stress build-up, thereby weakening the intervening barrier and increasing the seismic hazard. Moreover, the 1930 earthquake may not have fully released the accumulated elastic strain, as also observed in other continental strike-slip faults such as the 1812 and 1857 Fort Tejon earthquake pair on the San Andreas Fault<sup>45</sup>. This incomplete release would further reduce the effectiveness of the barrier<sup>34</sup>. Additionally, Coulomb stress transfer from historical earthquakes in the region may have further promoted rupture beyond the seismic gap9. Second, the nucleation occurred far north of this boundary in a more optimally prestressed fault section, allowing the rupture to propagate a long distance before hitting the southern boundary of the gap. Right-lateral slip along the extended rupture increased shear stress both within the barrier and further south, progressively weakening the stress barrier and facilitating the rupture breaching the seismc gap.

In summary, we have integrated seismological, geodetic and numerical methods to investigate the devastating  $2025 M_w 7.7$  Mandalay

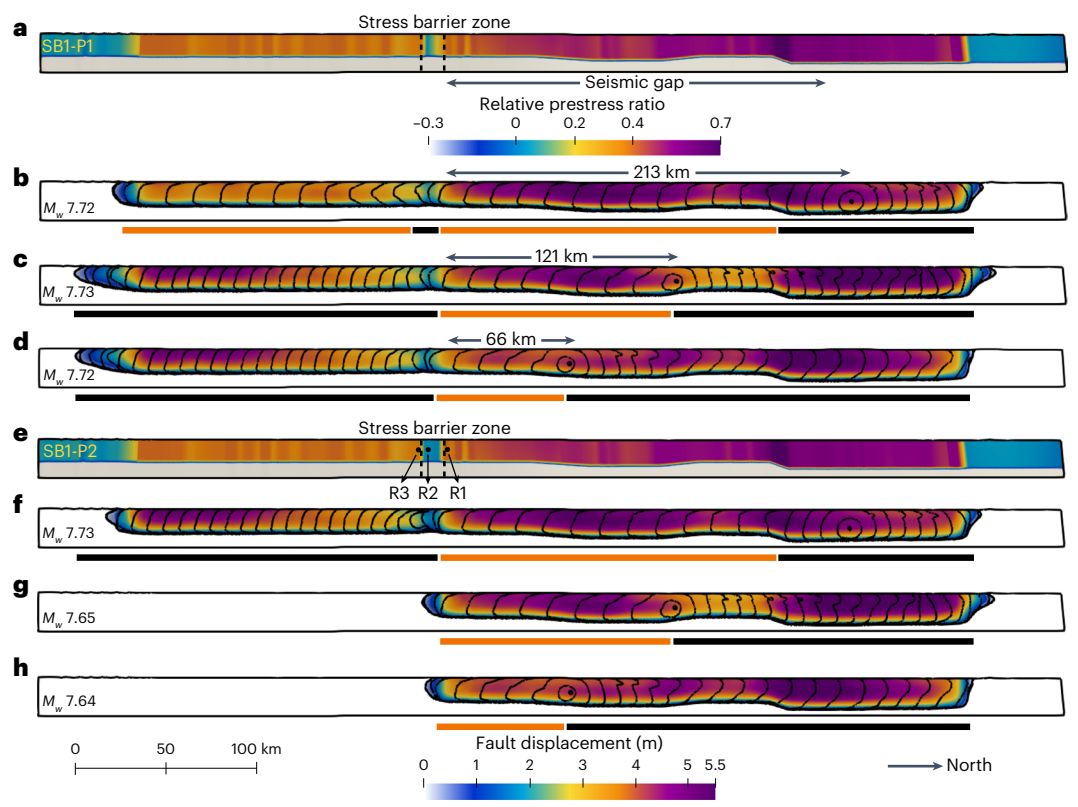


Fig. 5 | Nucleation location sensitivity tests. a, Relative prestress ratio of model SB1, with lower prestress in the stress barrier than the preferred model (Fig. 4b).  $\mathbf{b}-\mathbf{d}$ , Final slip for ruptures nucleating 213 km ( $\mathbf{b}$ ), 121 km ( $\mathbf{c}$ ) and 66 km ( $\mathbf{d}$ ) north of the stress barrier, respectively, with supershear rupture reaching the seismic gap. Black and orange lines below each scenario mark the extent of subshear and supershear rupture propagation along the fault, respectively. Black contours

show rupture fronts at 3-s intervals. The corresponding moment magnitude is stated in the bottom left of each panel.  $\mathbf{e}$ – $\mathbf{h}$ , As in  $\mathbf{a}$ – $\mathbf{d}$ , but with further reduced prestress in the stress barrier zone for examining alternative rupture behaviours. The black dots in  $\mathbf{e}$  show the locations of three on-fault receivers (R1, R2 and R3) for rupture-dynamics analysis near the barrier.

earthquake, revealing a two-stage rupture process. Although the event itself was not entirely unexpected—being located in a seismic gap that has not experienced large earthquakes for nearly 200 years—the rupture exceeded expectations by propagating not only through the entire gap but extending ~160 km beyond it. This led to more widespread ground shaking and infrastructural damage than previously anticipated for this segment. Fault segmentation and seismic gaps on geometrically simple strike-slip faults are observed elsewhere, such as for the San Andreas and North Anatolian Fault systems. Our simulations for the  $M_{\rm w}$  7.7 Mandalay temblor suggest that seismic gaps may not reliably reflect the size of future earthquakes. Instead, ruptures may cascade into adjacent fault segments 46,47, producing unexpectedly large and potentially more destructive events. For instance, the Marmara Sea seismic gap near Istanbul (last ruptured in 1509 and 1776), bounded by sections of the 1912  $M_{\rm w}$  7.3 Ganos rupture to the west and a sequence of large earthquakes in 1999 to the east<sup>48</sup>, may potentially produce a gap-breaching rupture that inflicts even higher seismic hazard to this densely populated region than the gap alone. Poorly constrained potential nucleation locations and highly variable rupture dynamics play a critical role in controlling slip distribution, rupture length, final magnitude and hence the resulting ground shaking for future earthquakes. Incorporating these dynamic factors into the analysis and interpretation of seismic gaps enhances and complements long-term seismic hazard assessment.

#### Online content

Any methods, additional references, Nature Portfolio reporting summaries, source data, extended data, supplementary information, acknowledgements, peer review information; details of author contributions

and competing interests; and statements of data and code availability are available at https://doi.org/10.1038/s41561-025-01861-7.

#### References

- Tapponnier, P., Peltzer, G., Le Dain, A., Armijo, R. & Cobbold, P. Propagating extrusion tectonics in Asia: new insights from simple experiments with plasticine. Geology 10, 611–616 (1982).
- Bertrand, G. & Rangin, C. Tectonics of the western margin of the Shan plateau (central Myanmar): implication for the India-Indochina oblique convergence since the Oligocene. J. Asian Earth Sci. 21, 1139–1157 (2003).
- Vigny, C. et al. Present-day crustal deformation around Sagaing fault, Myanmar. J. Geophys. Res. Solid Earth https://doi.org/ 10.1029/2002JB001999 (2003).
- Panda, D., Kundu, B., Gahalaut, V. K. & Rangin, C. Crustal deformation, spatial distribution of earthquakes and along strike segmentation of the Sagaing Fault, Myanmar. J. Asian Earth Sci. 166, 89–94 (2018).
- Tin, T. Z. H. et al. Present-day crustal deformation and slip rate along the southern Sagaing fault in Myanmar by GNSS observation. J. Asian Earth Sci. 228, 105125 (2022).
- Hurukawa, N. & Maung Maung, P. Two seismic gaps on the Sagaing Fault, Myanmar, derived from relocation of historical earthquakes since 1918. Geophys. Res. Lett. https://doi.org/ 10.1029/2010GL046099 (2011).
- Wang, Y., Sieh, K., Tun, S. T., Lai, K.-Y. & Myint, T. Active tectonics and earthquake potential of the Myanmar region. J. Geophys. Res. Solid Earth 119, 3767–3822 (2014).

- Engdahl, E. R. & Villaseñor, A. Global seismicity: 1900–1999.
  Int. Geophys. 81, 665–690 (2002).
- Xiong, X. et al. Coulomb stress transfer and accumulation on the Sagaing Fault, Myanmar, over the past 110 years and its implications for seismic hazard. Geophys. Res. Lett. 44, 4781–4789 (2017).
- Sykes, L. R. Aftershock zones of great earthquakes, seismicity gaps, and earthquake prediction for Alaska and the Aleutians. J. Geophys. Res. 76, 8021–8041 (1971).
- Lay, T. & Nishenko, S. P. Updated concepts of seismic gaps and asperities to assess great earthquake hazard along South America. Proc. Natl Acad. Sci. USA 119, e2216843119 (2022).
- McCann, W., Nishenko, S., Sykes, L. & Krause, J. Seismic gaps and plate tectonics: seismic potential for major boundaries. *Pure Appl. Geophys.* 117, 1082–1147 (1979).
- Nishenko, S. P. Circum-Pacific Seismic Potential: 1989–1999 (Springer, 1991).
- Métois, M. et al. Revisiting the North Chile seismic gap segmentation using GPS-derived interseismic coupling. Geophys. J. Int. 194, 1283–1294 (2013).
- Ergintav, S. et al. Istanbul's earthquake hot spots: geodetic constraints on strain accumulation along faults in the Marmara seismic gap. Geophys. Res. Lett. 41, 5783–5788 (2014).
- Kagan, Y. Y. & Jackson, D. D. Seismic gap hypothesis: ten years after. J. Geophys. Res. Solid Earth 96, 21419–21431 (1991).
- 17. Jackson, D. D. & Kagan, Y. Y. in Encyclopedia of Solid Earth Geophysics (ed. Gupta, H. K.) 53–56 (Springer, 2021).
- Lorito, S. et al. Limited overlap between the seismic gap and coseismic slip of the great 2010 Chile earthquake. *Nat. Geosci.* 4, 173–177 (2011).
- Subarya, C. et al. Plate-boundary deformation associated with the great Sumatra–Andaman earthquake. *Nature* 440, 46–51 (2006).
- Wyss, M. & Wiemer, S. How can one test the seismic gap hypothesis? The case of repeated ruptures in the Aleutians. *Pure Appl. Geophys.* 155, 259–278 (1999).
- Gabriel, A. K., Goldstein, R. M. & Zebker, H. A. Mapping small elevation changes over large areas: differential radar interferometry. J. Geophys. Res. Solid Earth 94, 9183–9191 (1989).
- Michel, R., Avouac, J.-P. & Taboury, J. Measuring ground displacements from SAR amplitude images: application to the Landers earthquake. *Geophys. Res. Lett.* 26, 875–878 (1999).
- Liu, J. et al. A method for measuring 3-D surface deformations with InSAR based on strain model and variance component estimation. *IEEE Trans. Geosci. Remote Sens.* 56, 239–250 (2018).
- Madariaga, R. High-frequency radiation from crack (stress drop) models of earthquake faulting. *Geophys. J. Int.* 51, 625–651 (1977).
- 25. Wang, X. et al. A 3-D shear wave velocity model for Myanmar region. J. Geophys. Res. Solid Earth 124, 504–526 (2019).
- Abrahamson, N. A., Silva, W. J. & Kamai, R. Summary of the ASK14 ground motion relation for active crustal regions. *Earthquake* Spectra 30, 1025–1055 (2014).
- Boore, D. M., Stewart, J. P., Seyhan, E. & Atkinson, G. M. NGA-West2 equations for predicting PGA, PGV, and 5% damped PSA for shallow crustal earthquakes. *Earthquake Spectra* 30, 1057–1085 (2014).
- Chiou, B. S.-J. & Youngs, R. R. Update of the Chiou and Youngs NGA model for the average horizontal component of peak ground motion and response spectra. *Earthquake Spectra* 30, 1117–1153 (2014).
- Campbell, K. W. & Bozorgnia, Y. NGA-West2 ground motion model for the average horizontal components of PGA, PGV, and 5% damped linear acceleration response spectra. *Earthquake Spectra* 30, 1087–1115 (2014).

- Dunham, E. M. & Bhat, H. S. Attenuation of radiated ground motion and stresses from three-dimensional supershear ruptures. J. Geophys. Res. Solid Earth https://doi.org/10.1029/2007JB005182 (2008).
- 31. Andrews, D. Ground motion hazard from supershear rupture. *Tectonophysics* **493**, 216–221 (2010).
- 32. Thingbaijam, K. K. S., Mai, P. M. & Goda, K. New empirical earthquake source-scaling laws. *Bull. Seismol. Soc. Am.* **107**, 2225–2246 (2017).
- Oglesby, D. D. & Mai, P. M. Fault geometry, rupture dynamics and ground motion from potential earthquakes on the North Anatolian Fault under the Sea of Marmara. *Geophys. J. Int.* 188, 1071–1087 (2012).
- Petrillo, G., Rosso, A. & Lippiello, E. Testing of the seismic gap hypothesis in a model with realistic earthquake statistics.
   J. Geophys. Res. Solid Earth 127, e2021JB023542 (2022).
- 35. Taufiqurrahman, T. et al. Dynamics, interactions and delays of the 2019 Ridgecrest rupture sequence. *Nature* **618**, 308–315 (2019).
- 36. Li, B., Gabriel, A.-A., Ulrich, T., Abril, C. & Halldorsson, B. Dynamic rupture models, fault interaction and ground motion simulations for the segmented Húsavík-Flatey fault zone, northern Iceland. *J. Geophys. Res. Solid Earth* **128**, e2022JB025886 (2023).
- 37. Choi, J.-H. et al. Geologic inheritance and earthquake rupture processes: the 1905 M≥8 Tsetserleg-Bulnay strike-slip earthquake sequence, Mongolia. *J. Geophys. Res. Solid Earth* **123**, 1925–1953 (2018).
- 38. Tsutsumi, H. & Sato, T. Tectonic geomorphology of the southernmost Sagaing fault and surface rupture associated with the May 1930 Pegu (Bago) earthquake, Myanmar. *Bull. Seismol. Soc. Am.* **99**, 2155–2168 (2009).
- Klinger, Y. Relation between continental strike-slip earthquake segmentation and thickness of the crust. J. Geophys. Res. Solid Earth https://doi.org/10.1029/2009JB006550 (2010).
- 40. Bouchon, M. & Vallée, M. Observation of long supershear rupture during the magnitude 8.1 Kunlunshan earthquake. *Science* **301**, 824–826 (2003).
- Dunham, E. M. & Archuleta, R. J. Evidence for a supershear transient during the 2002 Denali fault earthquake. *Bull. Seismol.* Soc. Am. 94, S256–S268 (2004).
- 42. Bouchon, M. et al. Faulting characteristics of supershear earthquakes. *Tectonophysics* **493**, 244–253 (2010).
- 43. Li, B. et al. Rupture dynamics and velocity structure effects on ground motion during the 2023 Türkiye earthquake doublet. Commun. Earth Environ. **6**, 228 (2025).
- 44. Andrews, D. Rupture velocity of plane strain shear cracks. *J. Geophys. Res.* **81**, 5679–5687 (1976).
- Smith, B. R. & Sandwell, D. T. A model of the earthquake cycle along the San Andreas fault system for the past 1,000 years.
   J. Geophys. Res. Solid Earth https://doi.org/10.1029/2005JB003703 (2006).
- Gabriel, A.-A., Garagash, D. I., Palgunadi, K. H. & Mai, P. M. Fault size-dependent fracture energy explains multiscale seismicity and cascading earthquakes. Science 385, eadj9587 (2024).
- Palgunadi, K. H., Gabriel, A.-A., Garagash, D. I., Ulrich, T. & Mai, P. M. Rupture dynamics of cascading earthquakes in a multiscale fracture network. J. Geophys. Res. Solid Earth 129, e2023JB027578 (2024).
- 48. Ambraseys, N. N. & Jackson, J. Seismicity of the Sea of Marmara (Turkey) since 1500. *Geophys. J. Int.* **141**, F1–F6 (2000).
- 49. Ferreira, A. M. & Woodhouse, J. H. Long-period seismic source inversions using global tomographic models. *Geophys. J. Int.* **166**, 1178–1192 (2006).
- Wang, Y. & Day, S. M. Effects of off-fault inelasticity on near-fault directivity pulses. J. Geophys. Res. Solid Earth 125, e2019JB019074 (2020).

**Publisher's note** Springer Nature remains neutral with regard to jurisdictional claims in published maps and institutional affiliations.

**Open Access** This article is licensed under a Creative Commons Attribution-NonCommercial-NoDerivatives 4.0 International License, which permits any non-commercial use, sharing, distribution and reproduction in any medium or format, as long as you give appropriate credit to the original author(s) and the source, provide a link to the Creative Commons licence, and indicate if you modified the licensed material. You do not have permission under this licence to share

adapted material derived from this article or parts of it. The images or other third party material in this article are included in the article's Creative Commons licence, unless indicated otherwise in a credit line to the material. If material is not included in the article's Creative Commons licence and your intended use is not permitted by statutory regulation or exceeds the permitted use, you will need to obtain permission directly from the copyright holder. To view a copy of this licence, visit <a href="https://creativecommons.org/licenses/by-nc-nd/4.0/">https://creativecommons.org/licenses/by-nc-nd/4.0/</a>.

© The Author(s) 2025

## **Methods**

#### Three-dimensional coseismic displacements

We processed two ascending and two descending tracks of Sentinel-1 SAR images to measure surface displacement along the satellite azimuth direction and the line-of-sight (LOS) direction using POT and InSAR techniques. To ensure complete coverage of the entire area of interest, each track consisted of four or five frames. First, we acquired adjacent frames on the same date within each track to create seamless images. Subsequently, using 30-m Shuttle Radar Topography Mission (SRTM) digital elevation model (DEM) data, we co-registered the last pre-event and first post-seismic images to generate interferograms. Both the InSAR interferograms and POT results made use of a multi-looking factor of  $10 \times 3$  (range × azimuth, ~40 m × 40 m) to enhance the signal-to-noise ratio and computational efficiency. Given the large deformation gradients near the fault zone, significant surface changes and substantial vegetation coverage in the affected area, we implemented the following quality control measures for the interferograms: (1) application of adaptive filtering (window size, 64; filter factor, 0.4); (2) masking of low-coherence areas using a coherence threshold of 0.5; (3) additional manual masking to preserve valid deformation signals while minimizing phase unwrapping errors. Following co-registration of the Sentinel-1 images but before POT processing, we performed de-ramping of the Sentinel co-registered images. The matching window size for POT was set to  $128 \times 64$  (range  $\times$  azimuth).

After obtaining four distinct deformation measurements (Supplementary Table 1; ascending/descending LOS and two azimuth directions) with substantially different imaging geometries, we resolved the 3D coseismic surface displacements using the SM-VCE method  $^{23,51}$ . The SM-VCE approach offers two key advantages: (1) incorporation of a strain model to account for deformation correlations within specified spatial windows; (2) utilization of variance component estimation to weight observations according to their noise levels, thereby optimally balancing the contributions of different deformation measurements. For 3D deformation estimation at each pixel, we applied the SM-VCE method within a 41 × 41-pixel window (-1.6 km × 1.6 km). Special consideration was given to near-fault areas, where pixels on the opposite side of the fault from the target pixel were excluded to prevent interference from mechanically heterogeneous displacement observations across the fault  $^{52}$ .

An aftershock ( $M_{\rm w}$  6.7) occurred only 12 min after the mainshock, and its deformation cannot be separated from the mainshock in the SAR data (Supplementary Table 1). The  $M_{\rm w}$  6.8 earthquake in 2012, slightly farther north, produced an -45-km-long rupture <sup>53</sup>. By comparison, assuming a shear modulus of 30 GPa and a depth extent of -16 km as used in our dynamic rupture model, the  $M_{\rm w}$  6.7 aftershock would be expected to generate -0.3-m surface displacement over a similar rupture length, which is negligible relative to the observed deformation. Moreover, no secondary faults were identified in the aftershock area, suggesting that both events ruptured the same fault, and thus the aftershock has little impact on our symmetry analysis.

# **Back-projection**

Back-projection utilizes the time-reversal property of curved wave-fronts recorded at seismic arrays to determine the time and location of sources that radiate high-frequency seismic energy<sup>54,55</sup>. With its computational efficiency, back-projection has become a standard tool for rapid and robust rupture-process imaging for large and moderate earthquakes<sup>56-58</sup>.

We utilized three large-scale seismic arrays—the European Array (EU), the Australian Array (AU) and the Alaskan Array (AK)—to perform back-projection to track the rupture process of the  $M_{\rm w}$  7.7 Mandalay earthquake. Stations were selected with epicentral distances of  $30-90^{\circ}$ . For each array, we applied cross-correlation within a 20-s time window around the direct *P*-wave arrival to identify stations with coherent waveforms. Only stations with an average cross-correlation

coefficient >0.6 were retained for back-projection analysis, resulting in 328, 132 and 167 stations for the EU, AU and AK arrays, respectively, at epicentral distances of 51.5–89.4° (EU), 30.9–80.3° (AU), 62.4–89.9° (AK) and azimuth ranges of 291.6–329° (EU), 105.6–162.6° (AU) and 7.3–41.6° (AK) (Supplementary Fig. 1).

The time shifts required to obtain the peak cross-correlation coefficients were used to empirically calibrate travel times relative to a 1D laterally homogeneous seismic velocity model, for which we adopt the Preliminary Reference Earth Model (PREM) $^{59}$ . For each array, we conducted back-projection using a 6-s sliding time window with a 0.1-s step size through the continuous waveform data to image the coseismic rupture evolution.

Given the steep dip of the Sagaing Fault and the limited vertical resolution inherent to teleseismic back-projection <sup>56,60</sup>, we projected the imaged rupture onto the mapped surface trace of the fault <sup>61</sup>, assuming the hypocentral depth reported by the Incorporated Research Institutions for Seismology (IRIS).

In complex rupture processes, factors such as rupture dynamics, attenuation, directivity and relative array locations can shape the dominant frequency energy recorded at different arrays, leading to array- and frequency-dependent rupture images  $^{\circ 2}$ . For the  $M_{\rm w}$  7.7 Mandalay earthquake, back-projection images of the EU and AK arrays show dominant northward rupture during the initial bilateral phase, whereas the AU array, located to the south, captures the southward rupture more clearly (Fig. 2). Therefore, integrating results across arrays and frequency provides a more comprehensive view of the rupture process.

#### **Bayesian geometry inversion**

Seismic waveforms and geodetic surface-displacement observations can be used to constrain fault geometry in a data-constrained inversion 63-65. For large earthquakes, the fault is usually represented as a series of rectangular subfaults, each defined by its strike, dip, rake, width, length and depth from the top fault edge (top depth) 66. Inverting the data for these parameters sequentially may introduce bias. We therefore adopted a full Bayesian inversion framework to simultaneously estimate the fault geometry parameters for all fault segments using a sequential Monte Carlo (SMC) sampling approach. This method efficiently explores the posterior distribution by drawing samples through a series of intermediate distributions and leveraging parallel computation on multiple central processing units (CPUs).

#### **Bayesian finite-fault inversion**

Given a known fault geometry, a finite-fault kinematic inversion resolves the rupture process by estimating the spatiotemporal slip distribution on the fault. Such slip models are often overparameterized relative to the data resolution, so regularization is required to stabilize the ill-posed inverse problem. In Bayesian inference, the regularization is imposed via a Gaussian prior with a covariance matrix derived from a Laplacian operator. The smoothing strength is controlled by a hyperparameter  $\alpha$ , inferred from the data. This regularization yields the posterior probability distribution function (PDF).

We used the Bayesian Earthquake Analysis Tool (BEAT)  $^{67,68}$  to estimate the posterior PDF of both the fault geometry and finite-fault model parameters  $\mathbf{m}$  ( $P(\mathbf{m}|\mathbf{d}_{\mathrm{obs}})$ ), based on the Bayesian theorem  $^{69}$  under the assumption of Gaussian distributed residuals  $\mathbf{r}_k(\mathbf{m})$ , expressed as

$$P(\mathbf{m}|\mathbf{d}_{\text{obs}}) \propto P(\mathbf{m}) \times \mathbf{\Pi}_{k=1}^{k} L(\mathbf{m}, \sigma_{k})$$
 (1)

$$L\left(\mathbf{m}, \sigma_{k}\right) = \frac{1}{\left(2\pi\sigma_{k}^{2}\right)^{N/2}\left|C_{k}\right|^{1/2}} \times \exp\left(\frac{1}{2\sigma_{k}^{2}}\left(\mathbf{r}_{k}\left(\mathbf{m}\right)\right)^{\mathsf{T}} C_{k}^{-1}\left(\mathbf{r}_{k}\left(\mathbf{m}\right)\right)\right)$$
(2)

Here,  $P(\mathbf{m})$  is the prior PDF,  $L(\mathbf{m}, \sigma_k)$  is the likelihood function, and  $\mathbf{r}_k(\mathbf{m}) = \mathbf{d}_{k,\text{obs}} - \mathbf{d}_k(\mathbf{m})$  denotes the residual between observed and synthetic data  $\mathbf{d}_k(\mathbf{m})$  for dataset k (for example, teleseismic and/or

coseismic surface deformation).  $C_k$  is the noise covariance matrix, and  $\sigma_k$  is a hierarchical scaling parameter estimating the residual standard deviation. We sampled the posterior using the SMC algorithm  $^{68,70}$ , which transitions through a sequence of intermediate distributions from the prior to the posterior (equation (1)).

For the inversion, we extended the fault plane from the surface to ~20-km depth along the dip direction and discretized it into subfaults with dimensions of  $4\times 4$  km², resulting in a total of 650 subfaults. Each subfault is characterized by four rupture parameters: slip amount in both the along-strike and down-dip directions, slip duration (rise time) and time of rupture-front arrival. Including additional nucleation point parameters, the hyperparameters of each dataset and the Laplacian smoothing factor, as well as hierarchical parameters for station correction, the inversion involves a total of 2,649 parameters, which are constrained by both geodetic and teleseismic observations. For each rupture parameter, we specified an 'uninformed' uniform prior distribution to allow both subshear and supershear rupture and the possibility for purely thrust and normal subfault dislocation.

#### Dynamic model

With the extended surface fracturing, the InSAR data clearly delineate the  $M_{\rm w}$  7.7 Mandalay earthquake's rupture trace. The observed asymmetry in surface-slip amplitude across the fault may result from a combination of non-vertical fault geometry and deviations from pure strike-slip motion <sup>43,71</sup>. The InSAR observations reveal asymmetry in the horizontal surface deformation that increases from south to north, consistent with results from Bayesian geometry inversion, indicating a shallower fault dip of the northern segment. Accordingly, we assigned an eastward dip angle of 70° in the north, transitioning to 80° towards the south.

For the dynamic rupture simulations, we constrained the seismogenic depths by recent GNSS studies that have revealed significant along-strike variations in geodetic slip rate and locking depth along the Sagaing Fault  $^5$ . In the northern Sagaing segment (SGs), the slip rate is estimated to be -18–24 mm yr  $^{-1}$ , with relatively deeper locking depths ranging from 15 to 25 km (refs. 3,4,72). However, Tin and colleagues  $^5$  suggest a shallower locking depth of -10 km in this region. The Meiktila segment (MTLs) exhibits a comparable slip rate to the SGs and a locking depth of -16 km. In contrast, reduced slip rates of 11 mm yr  $^{-1}$  have been suggested in the Nay Pyi Taw (NPTs) and Phyu (PYUs) segments. Further to the south, the Bago segment is characterized by a shallower locking depth of -10 km (refs. 5,73).

These variations in locking depth are consistent with the coseismic surface-displacement patterns revealed by InSAR and optical correlation data (Fig. 1b and Extended Data Fig. 2) and the slip distribution inferred from the Bayesian finite-fault inversion (Fig. 3a), which reveal two prominent slip patches in the SGs and MTLs. To incorporate along-strike variations of locking depth and long-term slip rate into the dynamic rupture simulations, we adjusted both the seismogenic depth and the stress parameter.

We followed the prestress loading approach of ref. 74 to initialize on-fault stress conditions. The orientation of the regional maximum horizontal compressive stress ( $\sigma_{\rm H_{max}}$ ) was set to N21° E, estimated from the World Stress Map<sup>75</sup>. We constrained the smallest and largest principal stress components by prescribing the maximum prestress ratio  $R_0$ , which varies between 0.3 and 0.82 along the ruptured fault, and is substantially lower outside (Supplementary Fig. 4a). Here,  $R_0$  = 1 corresponds to a critically stressed state for optimally oriented faults. Variations in both fault orientation and  $R_0$  yield different relative prestress ratios R along different fault sections. The relative prestress ratio R is defined as the ratio of the fault's dynamic stress drop to its breakdown strength drop, and is given by  $R = (\tau - \mu_{\rm d} \sigma_{\rm n}')/((\mu_{\rm s} - \mu_{\rm d})\sigma_{\rm n}')$  in which  $\tau$  is the shear stress,  $\mu_{\rm s}$  and  $\mu_{\rm d}$  are the static and dynamic friction coefficients, respectively, and  $\sigma_{\rm n}'$  is the effective normal stress, defined as the difference between the lithostatic stress and pore fluid pressure.

The fault's frictional behaviour was assumed to follow the linear slip-weakening law<sup>44</sup>. We then varied the friction parameters within physically reasonable ranges to identify the parameter set that generated the observed rupture breaching of the seismic gap, total rupture length, subshear to supershear transition, and best reproduced the geodetic and seismic observations. Through extensive but inevitably limited parameter-space exploration, we set the ratio of pore fluid pressure to lithostatic stress as y = 0.75, the static friction coefficient as  $\mu_s$  = 0.6, the dynamic friction coefficient as  $\mu_d$  = 0.25, and a spatially variable slip-weakening distance ( $D_c$ ) ranging from 0.1 to 0.8 m (Supplementary Fig. 4b) to allow for a transition from subshear to supershear rupture and generating the slip distribution indicated by back-projection<sup>76</sup>, geodetic observations and kinematic inversion. We note that tradeoffs among model parameters imply that an alternative set-up may lead to a similarly weak mechanical stress barrier and may be able to reproduce the observed rupture breaching and characteristics. The final relative prestress ratio and fault model is shown in Extended Data Fig. 2c.

To account for inelastic off-fault energy dissipation, we applied Drucker–Prager elasto-viscoplastic rheology The off-fault volumetric yielding behaviour is defined by two material parameters: the internal friction coefficient  $\mu_s^l = 0.65$ , slightly higher than the static friction coefficient  $\mu_s = 0.6$ , to reflect a lower resistance to react to a pre-existing fault Randthe plastic cohesion  $C_{\text{plast}}$ , which scales with the shear modulus  $\mu$  as  $C_{\text{plast}} = 0.0001\mu$  for weak shallow bedrock. The viscoplastic relaxation time  $T_v = 0.05$  s governs the rate at which stress relaxes to the yield surface and reaches the inviscid limit. This value ensures numerical stability and convergence of the simulation results under mesh refinement. In addition to geometric spreading, the seismic-wave energy decays with distance due to intrinsic attenuation. In our simulations, attenuation is characterized by the shear-wave quality factor  $Q_s = 50 \times V_s$  (where  $V_s$  is the shear-wave velocity in km s<sup>-1</sup>), and the compressional-wave quality factor  $Q_p = 2Q_s$  (ref. 80).

Following the time-dependent nucleation approach of the Statewide California Earthquake Center (SCEC) community benchmark <sup>81</sup> TPV24 (https://strike.scec.org/cvws/tpv24\_25docs.html), rupture is initiated kinematically by locally and gradually reducing the static friction coefficient  $\mu_s$  within a 1.5-km-radius nucleation patch <sup>82</sup>. The rupture initiation time T is given by

$$T = \begin{cases} \frac{r}{0.7V_r} + \frac{0.081r_{crit}}{0.7V_r} \left( \frac{1}{1 - (r/r_{crit})^2} - 1 \right), & r <= r_{crit} \\ 10^9, & r > r_{crit} \end{cases}$$
(3)

in which r is the radial distance (in metres in equation (3)) to the hypocentre,  $V_r$  is the prescribed rupture front velocity (set to 3,800 m s<sup>-1</sup>), and  $r_{crit}$  denotes the radius of the nucleation zone.

Regional topography and bathymetry are sourced from GeoMapApp<sup>83</sup> at a lateral resolution of -244 m. The on-fault mesh is refined to 150 m on average, progressively coarsening away from the fault using a gradation rate of 0.6. For synthetic ground-motion computations, we employed a more refined mesh within a designated region around the fault (Extended Data Fig. 6a), ensuring a global frequency resolution up to 1 Hz within 100 km of the fault surface. This meshing strategy yields a computational domain consisting of -208 million tetrahedral elements. The full 3D dynamic rupture and seismic-wave propagation simulations were then conducted using the open-source software Seis-Sol. A simulation of 200 s after nucleation requires 468.6K CPU hours on 256 nodes in Shaheen III.

# **Data availability**

The bathy-topography data in dynamic modelling is from GeoMapApp (www.geomapapp.org). The USGS kinematic finite-fault model is available from https://earthquake.usgs.gov/earthquakes/eventpage/us7000pn9s/finite-fault. The synthetic teleseismic waveform was

computed using the Incorporated Research Institutions for Seismology (IRIS) Synthetics Engine (https://ds.iris.edu/ds/products/syngine/). The aftershock catalogue and teleseismic data used for back-projection and kinematic finite-fault inversion are also from IRIS (https://ds.iris.edu/wilber3/find\_stations/11952284). The InSAR, optical correlation data and input files required to reproduce the earthquake simulations are available from Zenodo at https://zenodo.org/records/15482247 (ref. 84).

# **Code availability**

We used the open-source code SeisSol<sup>85</sup> for all dynamic rupture and ground-motion simulations (www.seissol.org), which is freely available to download from https://github.com/SeisSol/SeisSol/. The SM-VCE method used in this study is publicly available at https://zenodo.org/records/6346205 ref. 86. The Bayesian inversions for both fault geometry and kinematic finite-fault modelling were conducted using the Bayesian Earthquake Analysis Tool (BEAT) code available at https://pyrocko.org/beat. The figures were generated using the MATLAB, Paraview<sup>87</sup> and Generic Mapping Tools v6<sup>88</sup> from https://www.generic-mapping-tools.org/.

#### References

- 51. Liu, J., Jónsson, S., Li, X., Yao, W. & Klinger, Y. Extensive off-fault damage around the 2023 Kahramanmaraş earthquake surface ruptures. *Nat. Commun.* **16**, 1286 (2025).
- Hu, J. et al. Estimating three-dimensional coseismic deformations with the SM-VCE method based on heterogeneous SAR observations: selection of homogeneous points and analysis of observation combinations. *Remote Sens. Environ.* 255, 112298 (2021).
- Zufeng, C. et al. The 2012 Thabeikkjin (Myanmar) M 7.0 earthquake and its surface rupture characteristics. J. Geomech. 28, 169–181 (2022).
- Ishii, M., Shearer, P. M., Houston, H. & Vidale, J. E. Extent, duration and speed of the 2004 Sumatra–Andaman earthquake imaged by the Hi-Net array. *Nature* 435, 933–936 (2005).
- 55. Krüger, F. & Ohrnberger, M. Tracking the rupture of the  $M_w$ =9.3 Sumatra earthquake over 1,150 km at teleseismic distance. *Nature* **435**, 937–939 (2005).
- Ishii, M., Shearer, P. M., Houston, H. & Vidale, J. E. Teleseismic P wave imaging of the 26 December 2004 Sumatra-Andaman and 28 March 2005 Sumatra earthquake ruptures using the Hi-net array. J. Geophys. Res. Solid Earth https://doi. org/10.1029/2006JB004700 (2007).
- Li, B. & Ghosh, A. in *The Chile-2015 (Illapel) Earthquake and Tsunami* (eds Braitenberg, C. & Rabinovich, A. B.) 33–43 (Springer, 2017).
- 58. Zhang, L. et al. 2022  $M_{\rm w}$  6.6 Luding, China, earthquake: a strong continental event illuminating the Moxi seismic gap. Seismol. Res. Lett. **94**, 2129–2142 (2023).
- Dziewonski, A. M. & Anderson, D. L. Preliminary reference Earth model. *Phys. Earth Planet. Interiors* 25, 297–356 (1981).
- 60. Li, B., Gabriel, A.-A. & Hillers, G. Source properties of the induced  $M_L$  0.0–1.8 earthquakes from local beamforming and backprojection in the Helsinki area, southern Finland. Seismol. Res. Lett. **96**, 111–129 (2025).
- Mai, P. M. et al. The destructive earthquake doublet of 6 February 2023 in South-Central Türkiye and northwestern Syria: initial observations and analyses. Seismic Record 3, 105–115 (2023).
- Li, B. et al. Rupture heterogeneity and directivity effects in back-projection analysis. J. Geophys. Res. Solid Earth 127, e2021JB022663 (2022).
- Shimizu, K., Yagi, Y., Okuwaki, R. & Fukahata, Y. Construction of fault geometry by finite-fault inversion of teleseismic data. *Geophys. J. Int.* 224, 1003–1014 (2021).

- 64. Vasyura-Bathke, H. et al. Discontinuous transtensional rupture during the Mw 7.2 Gulf of Aqaba earthquake. Seismica https://doi.org/10.26443/seismica.v3i1.1135 (2024).
- 65. Suhendi, C. et al. Bayesian inversion and quantitative comparison for bilaterally quasi-symmetric rupture processes on a multi-segment fault in the 2021 Mw 7.4 Maduo earthquake. *Geophys. J. Int.* **240**, 673–695 (2024).
- 66. Haskell, N. Total energy and energy spectral density of elastic wave radiation from propagating faults. *Bull. Seismol. Soc. Am.* **54**, 1811–1841 (1964).
- Vasyura-Bathke, H. et al. BEAT: Bayesian Earthquake Analysis Tool v.1.0 https://doi.org/10.5880/fidgeo.2019.024 (GFZ Data Services, 2019).
- Vasyura Bathke, H. et al. The Bayesian Earthquake Analysis Tool. Seismol. Res. Lett. 91, 1003–1018 (2020).
- 69. Bayes, M. & Price, M. An essay towards solving a problem in the doctrine of chances. By the late Rev. Mr. Bayes, F.R.S. communicated by Mr. Price, in a letter to John Canton, A.M.F.R.S. *Philos. Trans.* (1683–1775) **53**, 370–418 (1763).
- 70. Del Moral, P., Doucet, A. & Jasra, A. Sequential Monte Carlo samplers. J. R. Stat. Soc. B Stat. Methodol. **68**, 411–436 (2006).
- 71. Aagaard, B. T., Hall, J. F. & Heaton, T. H. Effects of fault dip and slip rake angles on near-source ground motions: why rupture directivity was minimal in the 1999 Chi-Chi, Taiwan, earthquake. *Bull. Seismol. Soc. Am.* **94**, 155–170 (2004).
- Maurin, T. et al. First GPS results in northern Myanmar: constant and localised slip rate along the Sagaing fault. In EGU General Assembly Conference Abstracts Vol. 12, EGU2010-4544 (EGU, 2010).
- 73. Krishna, M. R. & Sanu, T. Seismotectonics and rates of active crustal deformation in the Burmese arc and adjacent regions. *J. Geodyn.* **30**, 401–421 (2000).
- 74. Ulrich, T., Gabriel, A.-A., Ampuero, J.-P. & Xu, W. Dynamic viability of the 2016  $M_w$  7.8 Kaikōura earthquake cascade on weak crustal faults. *Nat. Commun.* **10**, 1213 (2019).
- Heidbach, O. et al. World Stress Map Database Release 2016 https://doi.org/10.5880/WSM.2016.001 (GFZ Data Services, 2016).
- 76. Li, D. et al. The role of thermal pressurization in driving deep fault slip during the  $2021\,M_{\rm w}$  8.2 Chignik, Alaska megathrust earthquake. Preprint at *Earth ArXiv* https://doi.org/10.31223/X5PB2T (2025).
- Wollherr, S., Gabriel, A.-A. & Uphoff, C. Off-fault plasticity in three-dimensional dynamic rupture simulations using a modal Discontinuous Galerkin method on unstructured meshes: implementation, verification and application. *Geophys. J. Int.* 214, 1556–1584 (2018).
- Tong, H. et al. Mohr space and its application to the activation prediction of pre-existing weakness. Sci. China Earth Sci. 57, 1595–1604 (2014).
- Roten, D., Olsen, K., Day, S., Cui, Y. & Fäh, D. Expected seismic shaking in Los Angeles reduced by San Andreas fault zone plasticity. Geophys. Res. Lett. 41, 2769–2777 (2014).
- 80. Olsen, K. et al. ShakeOut-D: ground motion estimates using an ensemble of large earthquakes on the southern San Andreas fault with spontaneous rupture propagation. *Geophys. Res. Lett.* https://doi.org/10.1029/2008GL036832 (2009).
- 81. Harris, R. A. et al. The SCEC/USGS dynamic earthquake rupture code verification exercise. Seismol. Res. Lett. **80**, 119–126 (2009).
- 82. Harris, R. A. et al. A suite of exercises for verifying dynamic earthquake rupture codes. *Seismol. Res. Lett.* **89**, 1146–1162 (2018).
- 83. Ryan, W. B. et al. Global multi-resolution topography synthesis. Geochem. Geophys. Geosyst. https://doi.org/10.1029/2008GC002332 (2009).

- Mai, P. M. et al. Dataset and input files for the 2025 M<sub>w</sub>7.7 Myanmar earthquake. Zenodo https://doi.org/10.5281/zenodo.15482247 (2025).
- Gabriel, A.-A. et al. SeisSol (v1.3.2). Zenodo https://doi.org/ 10.5281/zenodo.15685917 (2025).
- 86. Jihong, L. et al. A SM-VCE method demo for calculating three-dimensional coseismic displacement of the 8 January 2022 *M*<sub>w</sub>6.7 Menyuan earthquake. *Zenodo* https://doi.org/10.5281/zenodo.6346205 (2022).
- 87. Ahrens, J., Geveci, B. & Law, C. ParaView: an end-user tool for large data visualization. *The Visualization Handbook* **717**, 8 (2005).
- 88. Wessel, P. et al. The Generic Mapping Tools version 6. Geochem. Geophys. Geosyst. **20**, 5556–5564 (2019).

# Acknowledgements

This work was supported by King Abdullah University of Science and Technology (KAUST, grant no. BAS/1/1339-01-01 to B.L., C.S. and P.M.M.). We acknowledge the KAUST Supercomputing Laboratory for providing computational resources on Shaheen III under project K10043. D.L. acknowledges funding from the New Zealand Ministry of Business, Innovation and Employment through the National Seismic Hazard Model Science Programme (contract no. 110316). Y.K. acknowledges funding from the European Research Council (ERC) under the BE\_FACT project (grant no. 101142339).

#### **Author contributions**

B.L., S.J. and P.M.M. conceived the study. B.L. performed the back-projection analysis and conducted the dynamic rupture

simulations. C.S. carried out the Bayesian kinematic finite-fault inversion, and D.L. contributed to the set-up and refinement of the dynamic models. J.L., A.D. and Y.K. processed the geodetic data. B.L., S.J., C.S., J.L., D.L., Y.K. and P.M.M. analysed the results and designed the figures. All authors contributed to the writing and revision of the manuscript.

## **Competing interests**

The authors declare no competing interests.

#### **Additional information**

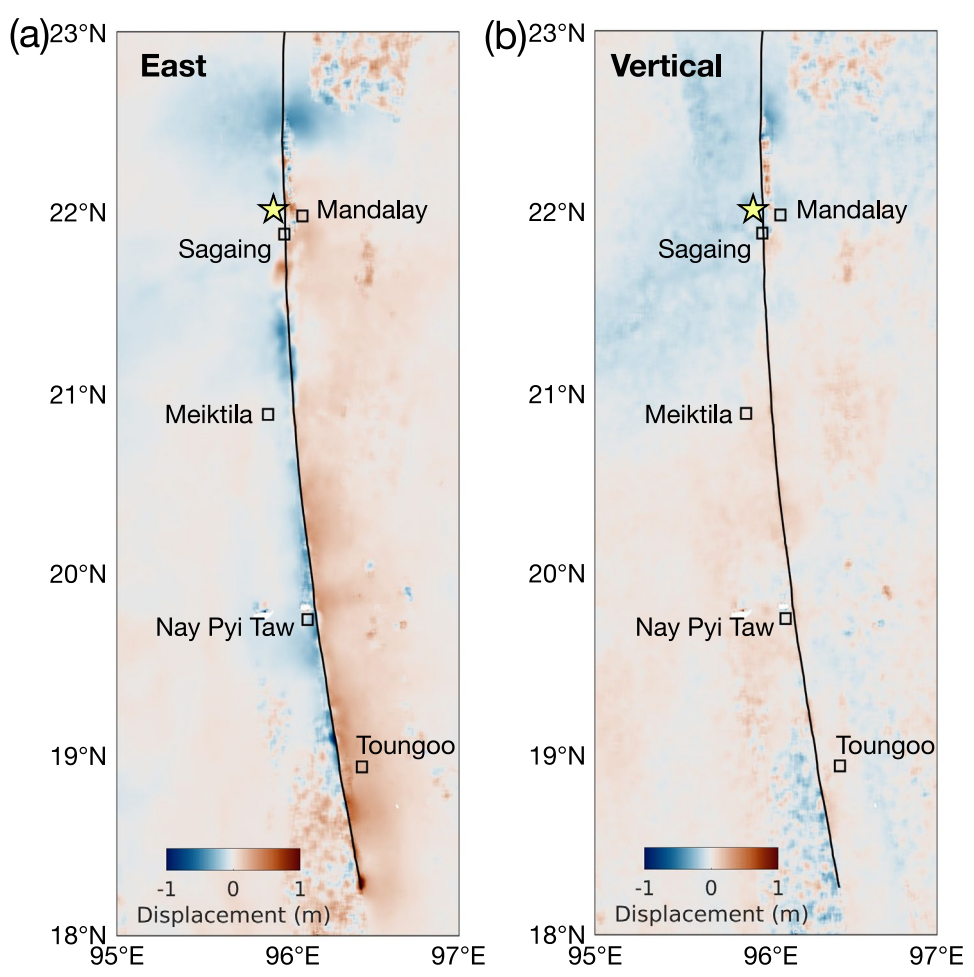
**Extended data** is available for this paper at https://doi.org/10.1038/s41561-025-01861-7.

**Supplementary information** The online version contains supplementary material available at https://doi.org/10.1038/s41561-025-01861-7.

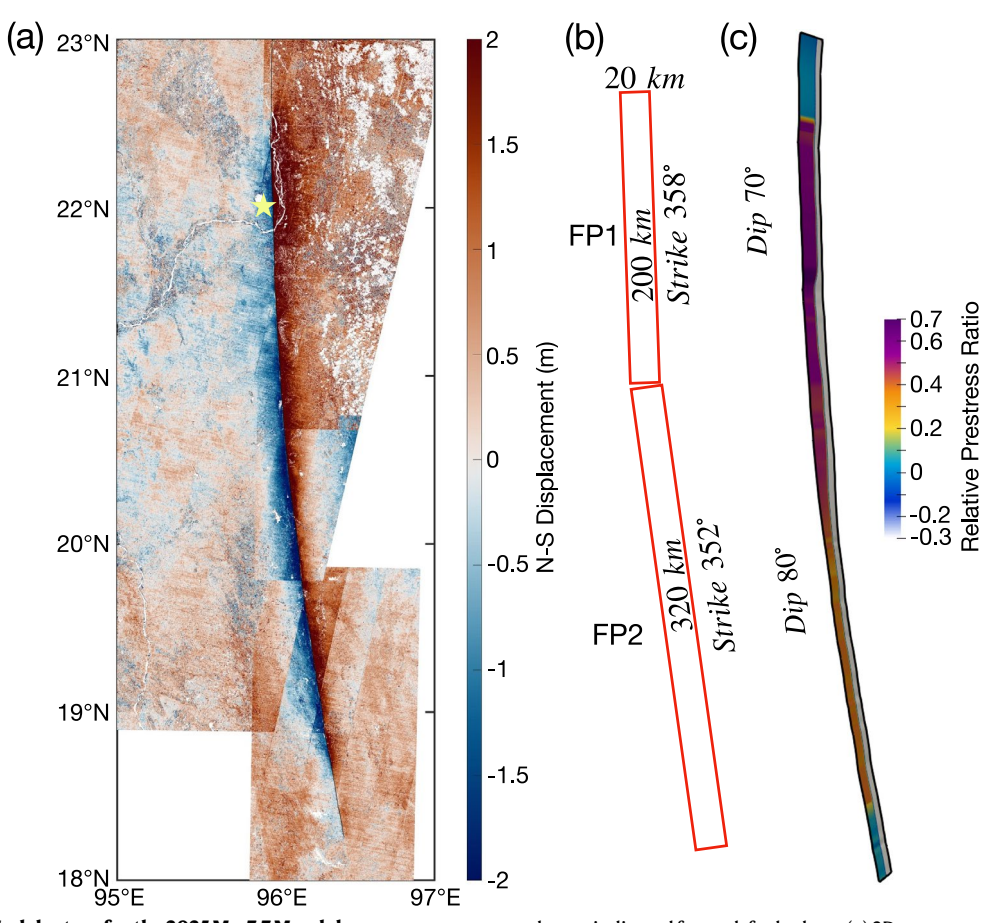
**Correspondence and requests for materials** should be addressed to Bo Li or Paul Martin Mai.

**Reviewer recognition** *Nature Geoscience* thanks the anonymous reviewer(s) for their contribution to the peer review of this work. Primary Handling Editor: Stefan Lachowycz, in collaboration with the *Nature Geoscience* team.

**Reprints and permissions information** is available at www.nature.com/reprints.

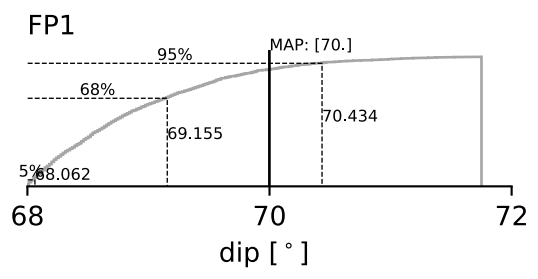


 $\textbf{Extended Data Fig. 1} | \textbf{Surface displacement field derived from SAR data.} \ \textbf{(a)} \ \textbf{The east component of surface displacement derived from SAR data.} \ \textbf{The smooth black} \\ \textbf{line indicates the mapped fault trace and the yellow star denotes the mainshock epicenter.} \ \textbf{(b)} \ \textbf{The vertical component of surface displacement derived from SAR data.} \\ \textbf{The vertical component of surface displacement derived from SAR data.} \ \textbf{(a)} \ \textbf{The vertical component of surface displacement derived from SAR data.} \\ \textbf{(b)} \ \textbf{The vertical component of surface displacement derived from SAR data.} \\ \textbf{(d)} \ \textbf{(d)}$ 

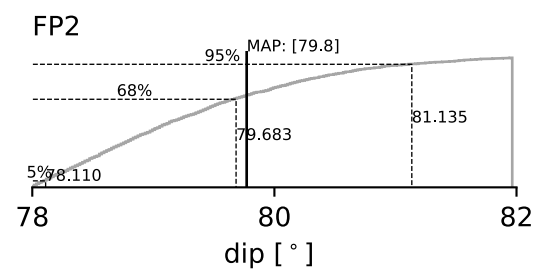


 $\label{lem:extended} \textbf{Data Fig. 2} \ | \ \textbf{Model set-up for the 2025 Mw 7.7 Mandalay} \\ \textbf{earthquake. (a)} \ \textbf{Optical satellite images correlation results (N-S component)} \\ \textbf{for Mw 7.7 Myanmar earthquake. (b)} \ \textbf{Map view of the two fault segments used} \\ \textbf{in the Bayesian finite-fault inversion. Segment dimensions, strike, and dip} \\ \\$ 

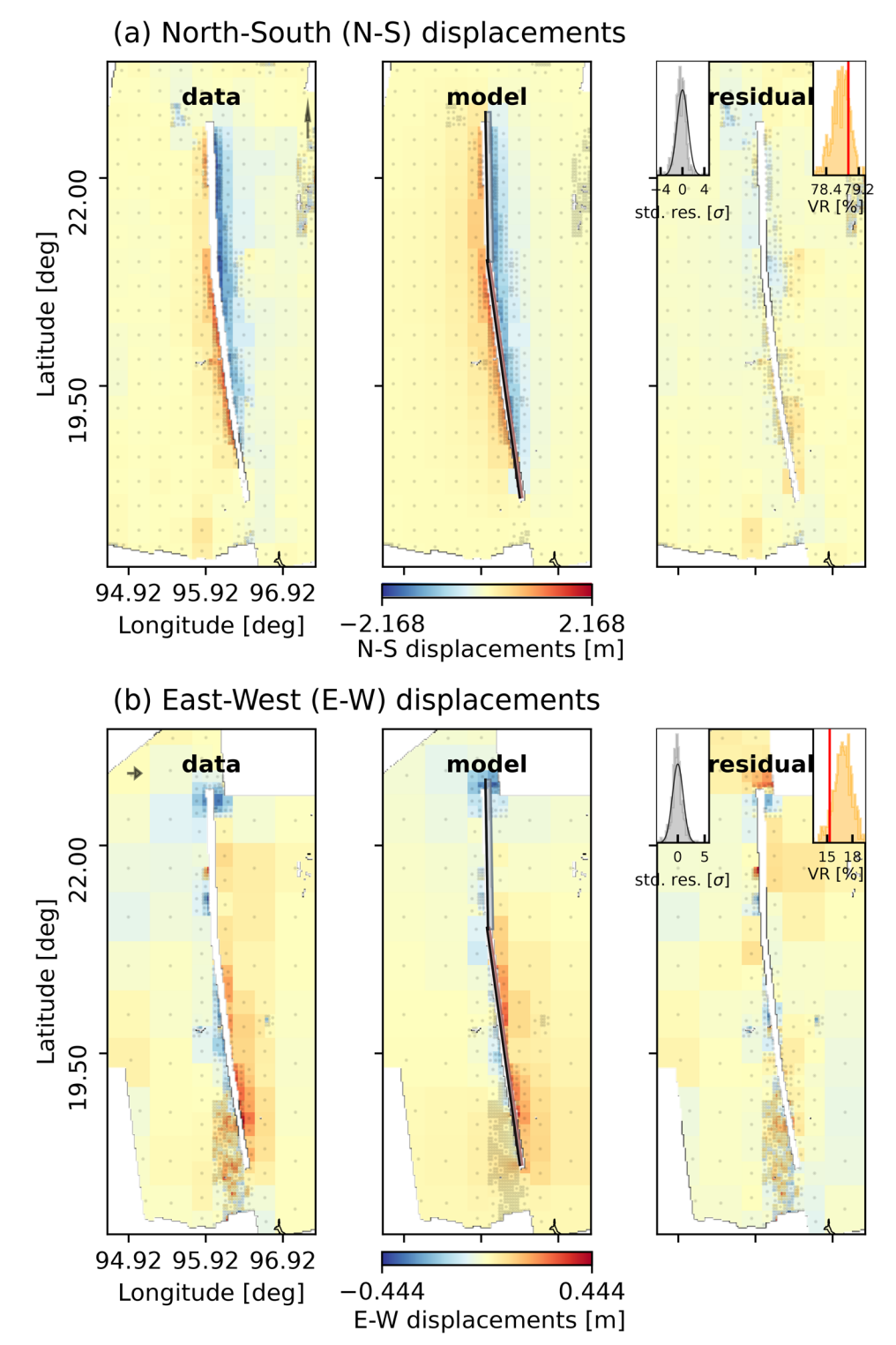
angles are indicated for each fault plane. ( $\mathbf{c}$ ) 3D prestress rendering of the dynamic fault model, represented by the relative prestress ratio (see details in **Methods:Dynamic model**).



**Extended Data Fig. 3 | Marginal cumulative distribution functions (CDFs) of fault dip angles from Bayesian inversion.** Left and right panels show the CDFs for fault segments FP1 and FP2, respectively. Curves represent the CDFs

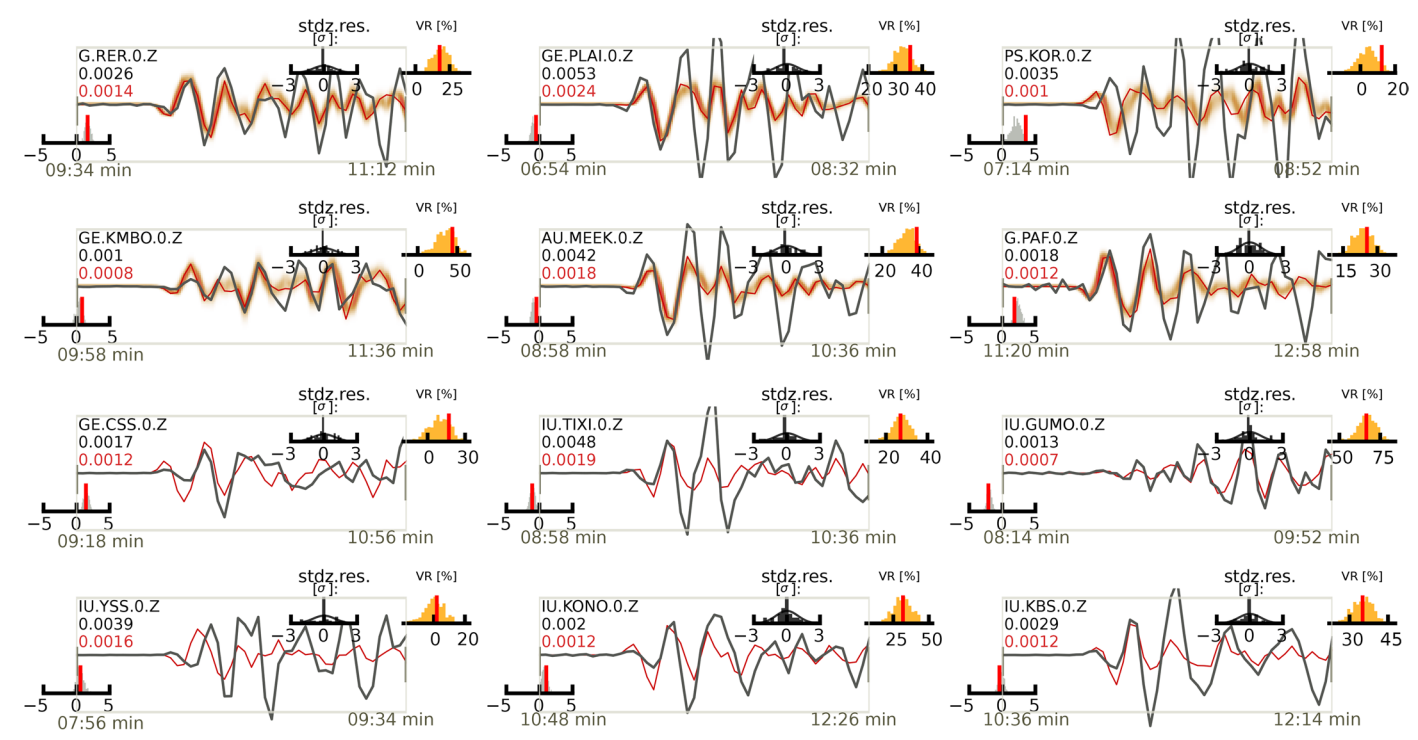


of the posterior distributions, with dashed lines indicating the 5%, 68%, and 95% percentile values. The vertical markers denote the Maximum A Posteriori (MAP) estimates of dip.



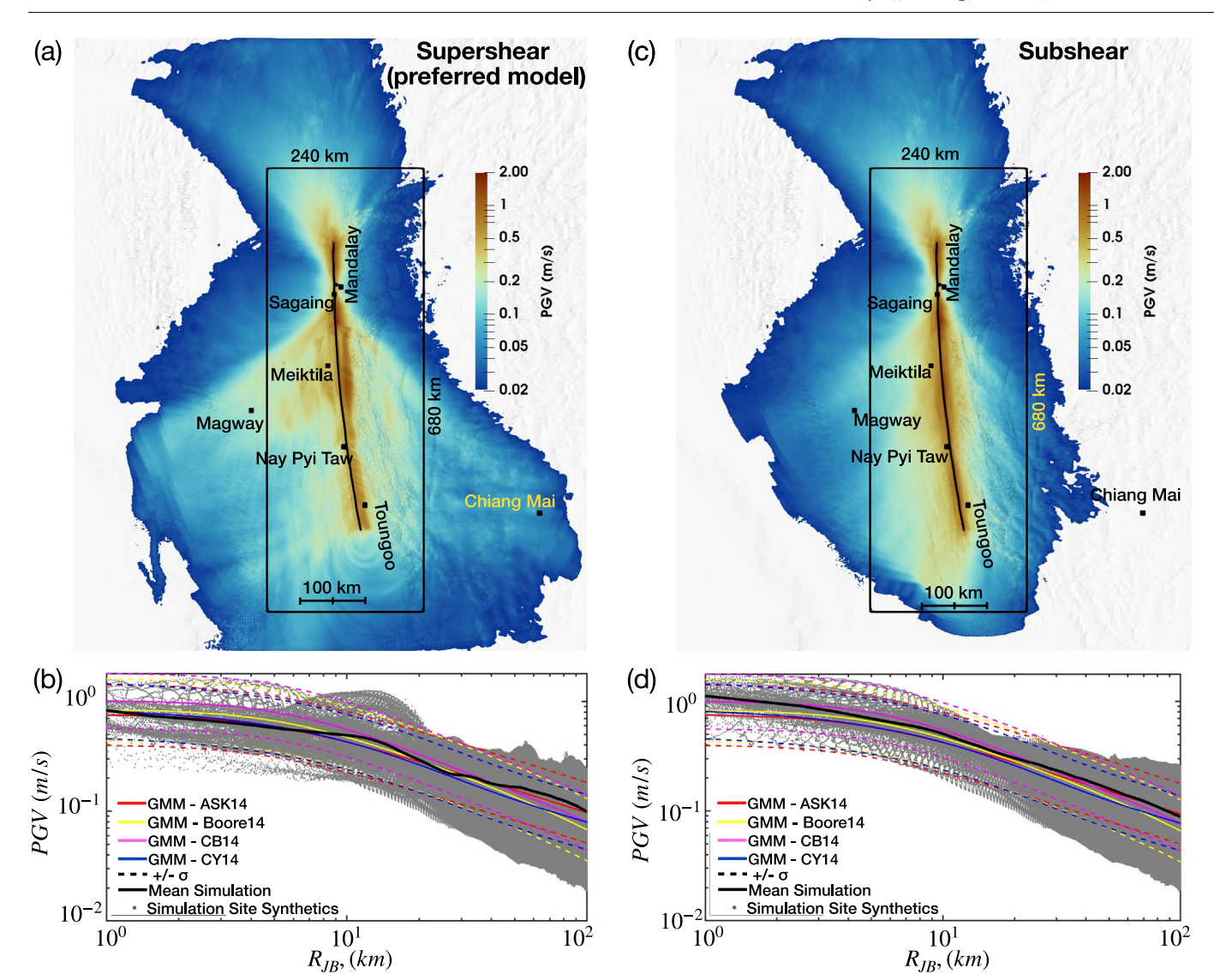
Extended Data Fig. 4 | Comparison of horizontal surface displacements between joint finite-fault inversion results and observations. (a) North–South displacements. (b) East–West displacements. The left panels show the downsampled observations, the middle panels display the corresponding

synthetic data, and the right panels present the residuals. Orange histograms in the top-right corners of the residual panels indicate the weighted variance reductions (VR), with red lines marking the maximum a posteriori (MAP) solution.



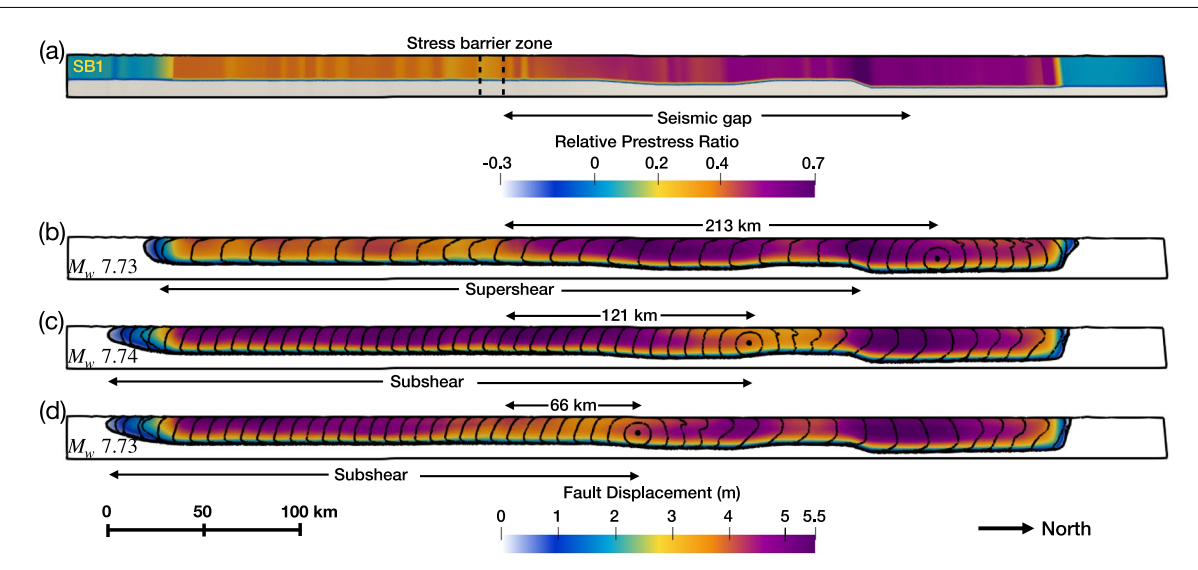
Extended Data Fig. 5 | Teleseismic waveform fits from the joint finite-fault inversion. Stations are shown in Figure S2. Gray and red lines show the filtered (0.05-0.2 Hz) observed and synthetic displacement waveforms, respectively. Black and red numbers in the top-left of each panel indicate the peak amplitudes (in cm) of the observed and synthetic traces. Light brown shading represents 500 synthetic waveform realizations sampled from the posterior distribution.

Each trace is labeled with the station name and time (in minutes) relative to the origin time. Gray and orange histograms in the lower-left and upper-right corners show the station-specific time shifts and weighted variance reductions (VR), respectively; red lines indicate the maximum a posteriori (MAP) solution. The black histogram in the top-middle of each panel shows the weighted residuals.



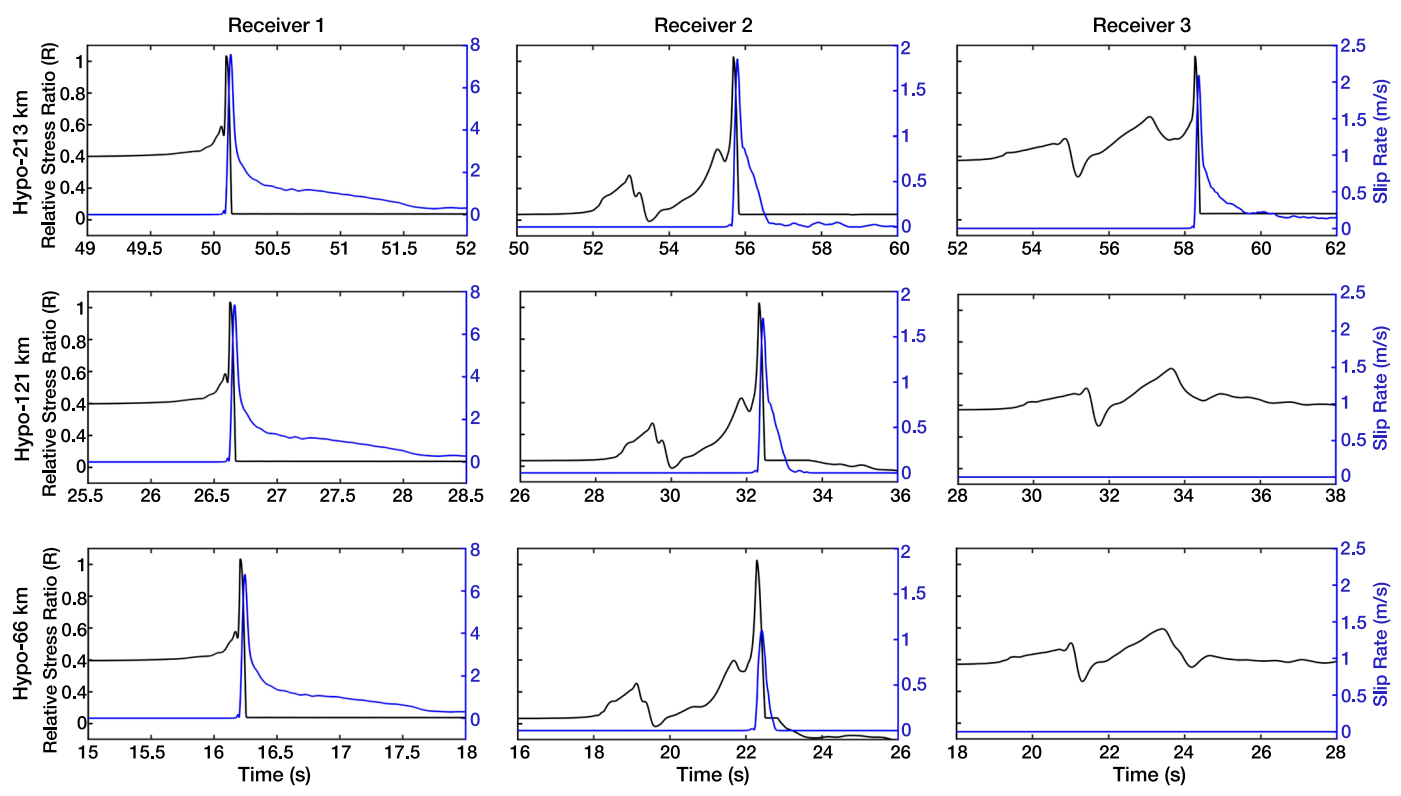
Extended Data Fig. 6 | Synthetic ground motions (PGV) from supershear and subshear rupture scenarios. (a) Synthetic ground motion (peak ground velocity (PGV), 1Hz resolution) of the preferred supershear rupture model. The black box outlines the refined mesh zone where globally 1Hz resolution is guaranteed. (b) Synthetic ground motion decay with distance compared to four empirical ground motion models [29-32]. Each dark gray dot represents a synthetic surface

site, while the black solid line shows the mean PGV decays with distance. Other colored solid and corresponding dashed lines represent the predictions and associated standard deviation from the empirical models, respectively. Panels ( $\mathbf{c}$ ) and ( $\mathbf{d}$ ) present the same quantities as ( $\mathbf{a}$ ) and ( $\mathbf{b}$ ), respectively, but for a purely subshear rupture scenario initiated at the same hypocenter as the preferred model, yielding a comparable magnitude of Mw 7.75.

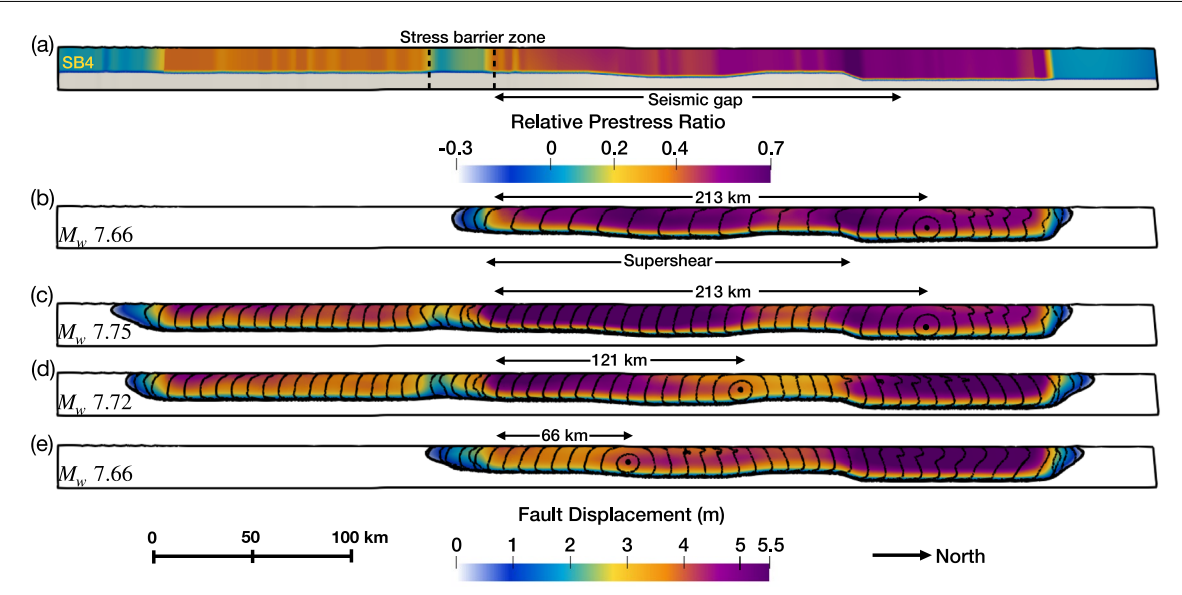


Extended Data Fig. 7 | Nucleation location sensitivity tests with the preferred model set-up. (a) Relative prestress ratio of the fault model (SB1) used as the preferred model for the Mw 7.7 Myanmar earthquake simulation. (b-d) Final fault slip for rupture scenarios initiated at 213 km, 121 km, and 66 km north of the

stress barrier zone, respectively. Black contours denote 3-second rupture time intervals. The resulting moment magnitude is indicated in the bottom-left of each panel.



**Extended Data Fig. 8** | **On-fault dynamics evolution.** Evolution of on-fault relative stress ratio (black) and slip rate (blue) at three receiver locations: north of the barrier (Receiver 1), within the barrier (Receiver 2), and south of the barrier (Receiver 3), for different nucleation scenarios. All simulations are based on prestress condition P2 (Fig. 5e) with barrier model SB1.



Extended Data Fig. 9 | Dynamic rupture scenarios illustrating the influence of rupture velocity and nucleation location. (a) Relative prestress ratio of the SB4 fault model used for nucleation sensitivity tests. (b) Final fault slip for a rupture nucleated 213 km north of the stress barrier, propagating as supershear when reaching the stress barrier zone. (c-e) Final fault slip for ruptures nucleated

 $213\,km$ ,  $121\,km$ , and  $66\,km$  north of the stress barrier, respectively, with subshear rupture between nucleation locations and the stress barrier zone. Black contours show rupture fronts at 3 s intervals. The corresponding moment magnitude is shown in the bottom-left of each panel.